

Copyright
by
Ryan Louis Swindeman
2015

The Thesis committee for Ryan Louis Swindeman
Certifies that this is the approved version of the following thesis:

**Iterative Seismic Data Interpolation Using Plane-wave
Shaping**

APPROVED BY

SUPERVISING COMMITTEE:

Sergey Fomel, Supervisor

Kyle Spikes

Omar Ghattas

**Iterative Seismic Data Interpolation Using Plane-wave
Shaping**

by

Ryan Louis Swindeman, B.S.

THESIS

Presented to the Faculty of the Graduate School of
The University of Texas at Austin
in Partial Fulfillment
of the Requirements
for the Degree of

Master of Science in Geological Sciences

THE UNIVERSITY OF TEXAS AT AUSTIN

May 2015

In memory of Niketa Dousias.

You've been my best friend since the beginning. I miss you more than I know how to express, but do I know that no matter what, we've still got each other's backs. Whenever I get weak, I can feel your strength augment my own. Thank you for your help; without it, this thesis would not be possible.

Acknowledgments

First and foremost, I'd like to thank my advisor Dr. Sergey Fomel. Both his intuition and understanding of geophysics have been nothing short of inspirational. My time spent at the University of Texas at Austin has been incredibly fulfilling because of his intelligence and patient guidance. We collaborated on Swindeman and Fomel (2015); Phillips et al. (2015), parts of which are used in Chapters 3 and 5. Coming from a background outside of this field, I exceptionally appreciate everything he has taught me, and without him, I'd be exactly where I started. Thank you.

Additional thanks to Karl Schleicher and Thomas Hess for the advice and expertise on handling the p-cable dataset and to the members of my committee members for their feedback and improvements to this thesis. To my family, friends, and Philip Guerrero: I appreciate your overwhelming support throughout these two years. You've made my experience very enjoyable and worthwhile.

The Madagascar software package is an open-source environment designed for reproducible research with multidimensional data. Additional thanks to the other software developers for their contributions to the workspace that I used to process the data in this thesis.

The Texas Consortium of Computational Seismology (TCCS) has been a wonderful environment for fostering the development of new ideas in geophysics. I'm thankful for the partial financial support for research from the sponsors of this consortium. To my colleagues in the consortium, your friendship and technical prowess have made my time here thoroughly enriching and mentally stimulating. I couldn't

ask for better coworkers and friends.

Iterative Seismic Data Interpolation Using Plane-wave Shaping

Ryan Louis Swindeman, M.S.Geo.Sci.

The University of Texas at Austin, 2015

Supervisor: Sergey Fomel

Geophysical applications often require finding an appropriate solution to an ill-posed inverse problem. An example application is interpolating irregular or sparse data to a regular grid. This data regularization problem must be addressed appropriately before many data processing techniques can begin. In this thesis, I investigate plane-wave shaping in two and three dimensions as a data regularization algorithm, which can be used for the interpolation of seismic data and images.

I use plane-wave shaping to interpolate several synthetic and field datasets and test its accuracy in image reconstruction. Because plane-wave shaping adheres to the direction of the local slopes of an image, the image-guided interpolation scheme attempts to preserve information of geologic structures. I apply several alternative interpolation schemes — formulated as an inverse problem with a convolutional op-

erator to constrain the model space — namely: plane-wave destruction, plane-wave construction, and prediction-error filters. Investigating their iterative convergence rates, I find that plane-wave shaping converges to a solution in fewer iterations than the alternative techniques. I find that the only required parameter for this method, the smoothing radius, is best chosen to be approximately the same size as the holes for missing-data problems. The optional parameter for edge padding is best selected as approximately half of the smoothing radius. Applications of this research project include potential applications in well-log interpolation, seismic tomography, and 5-D seismic data interpolation.

Table of Contents

Acknowledgments	v
Abstract	vii
List of Tables	x
List of Figures	xi
Chapter 1. Introduction	1
Chapter 2. Review of Existing Interpolation Strategies	5
Chapter 3. Seismic data interpolation using plane-wave shaping regularization	12
Chapter 4. Data Interpolation Experiments	25
Chapter 5. Sobel Filter	68
Chapter 6. Conclusions	72
Bibliography	75
Vita	81

List of Tables

- 4.1 Computational time dependence on smoothing radius for SeaBeam data 30

List of Figures

3.1	Synthetic example reproduced from Clapp et al. (2004). A 2-D slice of the quarterdome — Qdome — synthetic seismic image is given in (a) from which (b) the decimated data — wells — and (c) the dip field are derived. The nine traces were preserved in the application of the mask to produce the wells, and (c) is found by taking the local slope. . . .	16
3.2	2-D impulse responses. 50 spikes are placed randomly through the Qdome model and hit with the operators of (a) PWD, (b) PWC, and (c) PWS.	17
3.3	Convergence rate for 2-D synthetic example. This plot shows a comparison of the model error (2-norm) versus iteration number. The points denoted with “s” are derived from interpolation using PWS. The symbols “d” and “c” correspond to the same calculation using PWD and PWC, respectively.	18
3.4	Reconstruction of 2-D synthetic data with interpolation from (a) plane-wave destruction, (c) plane-wave construction, and (e) plane-wave shaping. Parts (b), (d), and (f) correspond to the respective data misfit, computed with $\ d - d_i\ _2^2$ for the true solution d and reconstruction d_i at iteration i . Convergence was reached after 55, 28 and 6 iterations, respectively.	19
3.5	3-D missing data fill. The original Qdome synthetic is shown in (a) and again in (b) with an ellipsoid-shaped hole of missing data. The reconstructions using PWS and PWD are shown in (c) and (d), respectively.	20
3.6	Dip field of 3-D Qdome image with ellipsoid-shaped hole with the (a) inline component and (b) cross-line component	21
3.7	3-D impulse response. 20 spikes are randomly placed in the 3-D qdome model. These peaks are smeared in a structure-guided fashion by 3-D PWS to produce this image.	22
3.8	Field data interpolation example. The original data is depicted in (a) and a mask, shown in (b), is applied to heavily decimate the input to create a set of wells. (c) shows the interpolated result of PWS, and (d) is the difference between the reconstruction and the original. The smallest-scale features and noise are removed as a result of the smoothing.	23
4.1	SeaBeam data	26

4.2	SeaBeam data mask	27
4.3	Estimated local slope of the SeaBeam data	27
4.4	SeaBeam reconstruction using (a) PWD, (b) PWC, and (c) PWS	29
4.5	SeaBeam interpolated image using PWS with a spatial padding of 1 on all sides and smoothing radii (r) of 30, 40, 50, 60, 70, and 80, respectively.	32
4.6	SeaBeam interpolated image using PWS with a spatial padding of 10 on all sides and smoothing radii (r) of 30, 40, 50, 60, 70, and 80, respectively.	33
4.7	SeaBeam interpolated image using PWS with a spatial padding of 20 on all sides and smoothing radii (r) of 30, 40, 50, 60, 70, and 80, respectively.	34
4.8	SeaBeam interpolated image using PWS with a spatial padding of 35 on all sides and smoothing radii (r) of 30, 40, 50, 60, 70, and 80, respectively.	35
4.9	SeaBeam interpolated image using PWS with a spatial padding of 50 on all sides and smoothing radii (r) of 30, 40, 50, 60, 70, and 80, respectively.	36
4.10	SeaBeam interpolated image using PWS with a spatial padding of 100 on all sides and smoothing radii (r) of 30, 40, 50, 60, 70, and 80, respectively.	37
4.11	Graph of computation time versus input data size for PWS	38
4.12	Destruction residual of PWS reconstruction	41
4.13	Initial model created by PWC	42
4.14	Depiction of (a) Original SeaBeam data, (b) PWS interpolation using smoothing radius of 70 and a padding size of 35 on all edges, and (c)–(f) random realizations of PWD with different seeds	43
4.15	Example REF Pattern	44
4.16	Example Spectrum of PEF	44
4.17	Reconstructions from the adjusted data using PEF-based interpolation without preconditioning	45
4.18	Reconstructions from the adjusted data using PEF-based interpolation with preconditioning	46
4.19	Map of the P-cable marine survey location	48
4.20	Diagram of P-cable acquisition system. Original picture by Geometrics Inc.	49
4.21	Stack of the P-cable seismic data. The large holes litter the image were created during the marine-data-acquisition phase of the project.	50

4.22	Mask of the original P-cable stack. White regions correspond to known data and have an integer value of 1. The holes in the data are black with an integer value of 0.	52
4.23	Calculated (a) inline dip and (b) cross-line dip	53
4.24	P-cable stack interpolation with smoothing radii of (a) 1 and (b) 5	54
4.25	P-cable stack interpolation with smoothing radii of (a) 10 and (b) 20	55
4.26	Original data flattened for display reference	56
4.27	Comparison of (a) and (b) interpolation using PWS with smoothing radius of (a) 1 and (b) 5	57
4.28	Comparison of interpolation using PWS with smoothing radius of (a) 10 and (b) 20	58
4.29	Comparison of timeslice 100 ms for (a) the original data, (b) the mask, and interpolation using PWS with a smoothing radius of (c) 1, (d) 5, (e) 10, and (f) 20.	59
4.30	P-cable stack interpolation using 3-D PWS.	60
4.31	P-cable stack interpolation using 3-D PWD.	61
4.32	Depiction of (a) the original mine blast data and (b) its associated mask	62
4.33	Estimated (a) inline dip and (b) cross-line dip	63
4.34	Missing-data reconstruction for the Blast dataset using (a) PWD-based and (b) PWS-based interpolation schemes	64
4.35	Panel view of interpolation with PWD. The left half (12 panels) of this image comes from frames of the original Blast data. The right 12 are taken after interpolating with a PWD-based approach.	65
4.36	Panel view of interpolation with PWS. The left half (12 panels) of this image comes from frames of the original Blast data. The right 12 are taken after interpolating with a PWS-based approach.	66

Chapter 1

Introduction

One of the most common problems that geologists and geophysicists routinely face is dealing with insufficient or irregular data. For instance, regions of coverage might be omitted during the acquisition of seismic data because of physical obstacles or hardware malfunction. For seismic data, experiments can produce only a discrete set of known values, and complication lies in the fact that there is an infinite number of ways to fill these gaps. A reasonable solution should be constrained to follow expected patterns. Data regularization (e.g., gridding) refers to the action of mapping and interpolating irregular data to a regular grid (Daley, 1993; Li and Gotze, 1999; Fomel, 2000). Throughout this thesis, I treat data regularization and interpolation as an inverse problem involving a convolutional operator (Claerbout, 1992, 1999; Claerbout and Fomel, 2014).

Data regularization has many important applications. One such use is finding missing information that was not gathered during seismic data acquisition, leaving behind irregularly sampled zones. In the case of geophysical exploration, returning to re-shoot seismic data or gathering more well logs can often be prohibitively expensive (Boreham et al., 1991; Stone, 1994). To make the best of this situation, data regularization can be used to synthetically fill holes in the data using information from known points. Another application is using data regularization to adjust irregularly

sampled data to a regular grid in order to prepare the data for further processing. This step is necessary, for example, to account for feathering of streamers during marine acquisition. Other potential applications include well-log interpolation (Clapp et al., 1998; Clapp, 2000), seismic tomography (Clapp et al., 2004; Woodward et al., 2008), and 5-D interpolation (Stanton and Sacchi, 2012; Gao et al., 2015).

Known problems exist with some popular interpolation schemes. For the iterative process associated with these methods, the convolutional operator should be appropriately anisotropic. By using an isotropic filter (such as a Laplacian), smearing happens in all directions equally, which may compromise the geologic structure of the initial image. The plane-wave techniques used in this thesis direct the regularization along the data's local slopes.

The main objective of this thesis is to investigate the strength of plane-wave shaping (PWS) as a data regularization technique, specifically through testing its ability to preserve structural information, provide a natural extension to higher dimensions, and converge in few iterations.

In order to test the effectiveness of the PWS algorithm, I directly compare it with several alternative interpolation methods by applying each to several datasets, both synthetic and real. In doing so, an analysis of the iterative convergence rate and reconstruction accuracy is performed. I test the interpolation schemes on 2-D and 3-D synthetic and field-data examples. Additionally, I investigate the sensitivity of PWS to external padding size, the smoothing radius parameter, and data-gap size. I explore the computational cost of the current implementation of PWS and its sensitivity to various parameters.

THESIS OUTLINE

Chapter 2 is dedicated to a review of several alternative interpolation strategies that historically preceded PWS and are used throughout this work as a basis for comparison. The schemes reviewed are PWD, plane-wave construction (PWC), and prediction-error filters (PEFs). I analyze the definition and theory of each.

In Chapter 3, I walk through the theory of shaping regularization (Fomel, 2007) from which PWS is derived. I examine the impulse response of PWS and compare it with those of the other methods. In a synthetic test, I create an artificial ellipsoid-shaped hole in the image and attempt to fill it without prior knowledge of the dip field. In the final tests, I heavily decimate seismic data to simulate well logs. Using the seismic dip field, these synthetic logs are interpolated and compared with the original seismic image for accuracy.

Chapter 4 tests the ability of PWS to interpolate data without a known solution. The missing pieces of three real datasets — the 2-D SeaBeam water-depth data, the 3-D P-cable seismic survey, and the 3-D Blast dataset — are constructed and analyzed. These tests illustrate how interpolation can be used in practical situations where missing data are simply unavailable.

In Chapter 5, I show the application of PWS to an image-guided implementation of the Sobel filter (Phillips et al., 2015), borrowed from an edge detector in the field of image processing. This procedure can be used as a way to efficiently detect faults. I also make some suggestions for other applications of PWS in future research.

In Chapter 6, I summarize the work presented in this thesis and discuss the results. I draw conclusions about the efficacy of PWS as an interpolation technique

in comparison with the alternative methods. The choice of a method should take into account the reconstruction accuracy/plausibility of the interpolated datasets along with the knowledge of iteration rate and parameter sensitivity.

Chapter 2

Review of Existing Interpolation Strategies

Many options exist in choosing an appropriate interpolation scheme for dealing with missing seismic data. The most common and simplest of these is interpolating in the inline or cross-line directions. Plane-wave shaping, an image-guided technique, has the added benefit of preserving structural information by moving along the local slopes of seismic events.

In this chapter, I discuss some of the interpolation strategies, alternative to plane-wave shaping (PWS), which together with PWS are used throughout this thesis. I discuss the history, benefits, and disadvantages of each of them and explore the theory from which their respective strengths and weaknesses arise.

INVERSE PROBLEMS

Each of the methods can be thought of as solving the inverse problem with objective function

$$\min_{\mathbf{m}} \|\mathbf{d} - \mathbf{L}\mathbf{m}\|_2^2. \quad (2.1)$$

The data, \mathbf{d} , that is given at the beginning is the “measured”, irregular data, possibly containing large holes. The goal is to find the model parameters in vector \mathbf{m} , (i.e., the regular data). In the case of missing data, the forward operator, \mathbf{L} , which maps

\mathbf{m} to \mathbf{d} , corresponds to simple masking.

Because of the ill-posed nature of many inverse problems, introducing a regularization term is necessary for constraining model parameters. An example implementation of Tikhonov regularization adds a term to the objective function to penalize steep slopes in the model space, morphing Equation 2.1 into

$$\min_{\mathbf{m}} \|\mathbf{d} - \mathbf{L}\mathbf{m}\|_2^2 + \epsilon \|\nabla\mathbf{m}\|_2^2, \quad (2.2)$$

in order to produce a smoother model. The sensitivity of this smoothing effect is controlled by regularization parameter ϵ . Two possible choices for finding this parameter are the Morozov discrepancy criterion (Morozov, 1971) or the L-curve method (Hansen, 1992). The Morozov discrepancy criterion states

$$\|\mathbf{d} - \mathbf{L}\mathbf{m}_\alpha\| \leq \delta, \quad (2.3)$$

meaning that the apparent noise level δ bounds the norm of the misfit. The L-curve method populates a plot of $\|\mathbf{m}\|$ versus the norm of the misfit. Then, ϵ is selected near the elbow that typically appears in this plot relatively close to the origin.

Everywhere that a solution to the inverse problem is attempted iteratively, there exists a choice in algorithm to approach the minimum. In PWS, a conjugate-gradient (CG) scheme is employed (Hestenes and Stiefel, 1952).

When dealing with an over-determined system, the least-squares solution takes the form

$$\hat{\mathbf{m}} = (\mathbf{L}^T\mathbf{L})^{-1} \mathbf{L}^T \mathbf{d}, \quad (2.4)$$

where \mathbf{L}^T is the adjoint of \mathbf{L} , and $\hat{\mathbf{m}}$ is a vector of the estimated model parameters.

Currently four choices of regularization techniques are available for inversion with seismic data: Tikhonov regularization (Tikhonov, 1963), model reparameterization (Harlan, 1995), shaping regularization (Fomel, 2007), and sparse regularization (Tibshirani, 1996). These styles of regularization are closely related to the interpolation techniques used in this thesis, barring sparsity, which itself is a very active area of research with application in many fields (Bhandari et al., 2014; Ding and Selesnick, 2015; Luo et al., 2015).

PREDICTION-ERROR FILTERS

Prediction-error filters (PEFs) are applied using the simple convolution equation

$$\mathbf{f} * \mathbf{d} = \mathbf{r}, \tag{2.5}$$

or equivalently in matrix form,

$$\mathbf{F}\mathbf{d} = \mathbf{r}, \tag{2.6}$$

for the filter \mathbf{f} and prediction-error (residual) \mathbf{r} , which is minimized in the least-squares sense. By applying a PEF, the predictable parts of the data are removed, leaving only the unpredictable signal, meaning the error components are uncorrelated, so

$$\mathbf{I} = E[\mathbf{r}\mathbf{r}^T] = E[\mathbf{F}\mathbf{d}\mathbf{d}^T\mathbf{F}^T] = \mathbf{F}E[\mathbf{d}\mathbf{d}^T]\mathbf{F}^T, \tag{2.7}$$

leading to

$$E[\mathbf{d}\mathbf{d}^T] = (\mathbf{F}^T\mathbf{F})^{-1}, \tag{2.8}$$

for $E[\mathbf{d}\mathbf{d}^T]^{-1}$ the inverse of the autocorrelation or covariance matrix of \mathbf{d} .

In practice PEFs are used for predictive deconvolution to remove the predictable events (such as multiples) from seismic data and leave behind the reflections (Yilmaz, 2001).

PLANE-WAVE DESTRUCTION

The original plane-wave destruction (PWD) filters were developed by Claerbout (1992). Applying PWD filters has been shown to be a powerful tool for slope estimation, noise attenuation, fault detection, and data interpolation (Fomel, 2002). PWD filters are the time-distance (T-X) analogs of frequency-distance (F-X) PEFs. The derivation of this technique, outlined by Fomel (2002), is based on the local plane-wave equation (Claerbout, 1992):

$$\frac{\partial P}{\partial x} + \sigma \frac{\partial P}{\partial t} = 0, \quad (2.9)$$

for a wavefield $P(t, x)$ and local slope σ . Under the Fourier transform, this becomes

$$\frac{d\hat{P}}{dx} + i\omega\sigma\hat{P} = 0 \quad (2.10)$$

$$\hat{P}(x) = \hat{P}(0) e^{i\omega\sigma x}, \quad (2.11)$$

in the frequency domain for stationary σ . Noticing the form of this solution, the operator that carries x to its neighbor (for integer x) is just a multiplicative factor of the complex exponential, from

$$\hat{P}(x) = \hat{P}(0) e^{i\omega\sigma(x-1)} e^{i\omega\sigma} = e^{i\omega\sigma} \hat{P}(x-1), \quad (2.12)$$

which represents a two-point F-X PEF. In extension to the time domain, the analog of the complex exponential is convolving with an all-pass filter which amounts to applying 2-D filters (in Z-transform notation) of the form

$$A(Z_t, Z_x) = 1 - Z_x \frac{B(Z_t)}{B(1/Z_t)}, \quad (2.13)$$

where filter A corresponds to a plane wave and B is a centered three-point filter. In the matrix form, this can be visualized more intuitively as a matrix multiplication

$$\mathbf{D} = \begin{bmatrix} \mathbf{I} & 0 & 0 & \cdots & 0 \\ -\mathbf{P}_{1,2} & \mathbf{I} & 0 & \ddots & \vdots \\ 0 & -\mathbf{P}_{2,3} & \mathbf{I} & \ddots & 0 \\ \vdots & \ddots & \ddots & \ddots & 0 \\ 0 & \cdots & 0 & -\mathbf{P}_{N-1,N} & \mathbf{I} \end{bmatrix}$$

for prediction operator $\mathbf{P}_{a,a+1}$, mapping a trace to an adjacent trace (Fomel and Guitton, 2006; Fomel, 2010). How an adjacent trace is predicted and subtracted from the original is now evident. In that sense, PWD can be thought of as an analog of differentiation based on the corresponding Z-transform (Fomel and Claerbout, 2003).

Fomel (2002) describes estimating local slopes, ultimately by means of solving an inverse problem by minimizing in a least-squares sense the difference

$$\frac{d\mathbf{C}}{d\sigma}(\sigma_0)\Delta\sigma\mathbf{d} - \mathbf{C}(\sigma_0)\mathbf{d}, \quad (2.14)$$

which is a linearization of the destruction objective, $\mathbf{C}(\sigma) \approx 0$, for σ (slope) using \mathbf{d} (data) and \mathbf{C} (operator of convolving the data with the PWD filter). This is the dip estimation technique used throughout the thesis to estimate the local slope of data and images. PWD can be used as a model-roughening operator (\mathbf{G}) in Tikhonov's regularization with objective function

$$\|\mathbf{d} - \mathbf{L}\mathbf{m}\|_2^2 + \|\mathbf{G}(\mathbf{m})\|_2^2, \quad (2.15)$$

where \mathbf{L} is the forward modeling operator for \mathbf{m} , the vector of model parameters, and \mathbf{d} is the data. $\mathbf{G}(\mathbf{m})$ replaces the gradient operator in Equation 2.2.

Recent advancements in PWD filters have been made with the advent of accelerated PWD (Chen et al., 2013a) and omnidirectional PWD (Chen et al., 2013b).

PLANE-WAVE CONSTRUCTION

Plane-wave construction (PWC) was introduced by Fomel and Guitton (2006) as a strategy for producing data in a local-slope direction. PWC has been used as an effective tool for interpolation of missing data, coherency enhancement, multiple suppression, and velocity estimation. The PWC operator is defined simply as the inverse of the PWD operator. In other words, traces (\mathbf{s}) are formed from construction ($\mathbf{C} \equiv \mathbf{D}^{-1}$) of the destruction residual (\mathbf{r}):

$$\mathbf{r} = \mathbf{D}\mathbf{s} \Leftrightarrow \mathbf{s} = \mathbf{C}\mathbf{r}. \quad (2.16)$$

In matrix form, the construction operator is

$$\mathbf{C} = \begin{bmatrix} \mathbf{I} & 0 & 0 & \cdots & 0 \\ -\mathbf{P}_{1,2} & \mathbf{I} & 0 & \ddots & \vdots \\ 0 & -\mathbf{P}_{2,3} & \mathbf{I} & \ddots & 0 \\ \vdots & \ddots & \ddots & \ddots & 0 \\ 0 & \cdots & 0 & -\mathbf{P}_{N-1,N} & \mathbf{I} \end{bmatrix}^{-1} \quad (2.17)$$

$$= \begin{bmatrix} \mathbf{I} & 0 & 0 & \cdots & 0 \\ \mathbf{P}_{1,2} & \mathbf{I} & 0 & \ddots & \vdots \\ \mathbf{P}_{1,3} & \mathbf{P}_{2,3} & \mathbf{I} & \ddots & 0 \\ \vdots & \ddots & \ddots & \ddots & 0 \\ \mathbf{P}_{1,N} & \cdots & \mathbf{P}_{N-2,N} & \mathbf{P}_{N-1,N} & \mathbf{I} \end{bmatrix}, \quad (2.18)$$

taking the form of a blocked lower triangular matrix. In this form, applying PWC can look like recursive integration. PWC can be used as a tool for model reparameterization. Fomel and Guitton (2006) use PWC operator \mathbf{C} to act on the reparameterized model \mathbf{p}

$$\mathbf{d} = \mathbf{L}\mathbf{m} = \mathbf{L}\mathbf{C}\mathbf{p}. \quad (2.19)$$

I use this guidance to rederive PWC by addressing this problem as an under-determined least squares optimization. Under-determined least squares reparameterization works

by substitution of an attempted solution

$$\mathbf{p} = (\mathbf{LC})^T \mathbf{y}, \quad (2.20)$$

for an unknown vector \mathbf{y} into

$$\mathbf{d} = \mathbf{LCp} = \mathbf{LC}(\mathbf{LC})^T \mathbf{y} = \mathbf{LCC}^T \mathbf{L}^T \mathbf{y}, \quad (2.21)$$

which, when inverted with a regularization parameter ϵ , becomes

$$\mathbf{y} = (\mathbf{LCC}^T \mathbf{L}^T + \epsilon^2 \mathbf{I})^{-1} \mathbf{d} \quad (2.22)$$

$$\Rightarrow \mathbf{p} = (\mathbf{LC})^T (\mathbf{LCC}^T \mathbf{L}^T + \epsilon^2 \mathbf{I})^{-1} \mathbf{d} = \mathbf{C}^T \mathbf{L}^T (\mathbf{LCC}^T \mathbf{L}^T + \epsilon^2 \mathbf{I})^{-1} \mathbf{d} \quad (2.23)$$

$$\Rightarrow \mathbf{m} = \mathbf{CC}^T \mathbf{L}^T (\mathbf{LCC}^T \mathbf{L}^T + \epsilon^2 \mathbf{I})^{-1} \mathbf{d}. \quad (2.24)$$

This formulation of the model parameters provides a solution to the inverse problem.

Chapter 3

Seismic data interpolation using plane-wave shaping regularization

1

The problem with interpolating insufficient, irregularly sampled data is that there exist infinitely many solutions. When solving ill-posed inverse problems in geophysics, one can apply regularization to constrain the model space in some way. I propose to use plane-wave shaping in iterative regularization schemes. By shaping locally planar events according to the local slope, regularization can effectively interpolate in the structure-oriented direction and preserve the most geologic dip information. In my experiments, this type of interpolation converged in fewer iterations than alternative techniques. The proposed plane-wave shaping could have potential applications in other problems such as seismic tomography and well-log interpolation.

INTRODUCTION

Choosing the most appropriate interpolation scheme to cope with insufficient seismic data can be challenging. Often the simplest direction in which I choose to interpolate is the inline or cross-line direction. This strategy can be improved by interpolating along seismic horizons to preserve structural information.

¹Parts of this chapter appear in (Swindeman and Fomel, 2015)

Previous work taking geologic structure into account for tomography applications was done by Clapp et al. (2004) by using space-varying steering filters. Structure-oriented filters can be applied to a seismic image to improve interpretation (Fehmers and Höcker, 2003; Liu et al., 2010). Blended-neighbor interpolation was developed by Hale (2009, 2010). This method interpolates borehole data across seismic data to a 3-D grid and can be extended to the image domain (Naeini and Hale, 2014).

Regularization is a technique to constrain model parameters for inversion. Solving ill-posed, seismic inverse problems offers several choices in the form of regularization (Engl et al., 1996; Zhdanov, 2002). The well-known and widely used Tikhonov regularization (Tikhonov, 1963) is reliable but can cause slow convergence because it conflicts with the main goal of the data misfit term in the objective function (Harlan, 1995). For seismic events with a dominant local slope, an appropriate operator for Tikhonov regularization is plane-wave destruction (PWD). Model reparameterization, another regularization style, encourages a certain behavior by applying a preconditioning operator (Fomel and Claerbout, 2003). The analog for local plane-wave events is plane-wave construction (PWC) which is the mathematical inverse of the PWD operator (Fomel and Guitton, 2006). A simpler form of PWC is the steering filters of Clapp et al. (1998, 2004). PWD and PWC are described in detail in the previous chapter.

In this chapter, I investigate a different form of regularization: plane-wave shaping (Fomel, 2007) and investigate the properties of plane-wave shaping (PWS) regularization on a 2-D synthetic example, a 3-D synthetic example, and 3-D field data. I heavily decimate the input data and test several interpolation schemes. By comparing the data misfit as a function of iteration number, I find that using shaping

regularization along structure achieves an accurate solution in fewer iterations than the alternative regularization methods, PWD and PWC.

Because of the generality of using plane-wave shaping to implement regularization, this method could have utility in many areas of geophysics. Estimating a trustworthy velocity model in reflection seismology is one such inverse problem (Clapp et al., 2004; Woodward et al., 2008).

PLANE-WAVE SHAPING

The general formulation of linear shaping regularization is (Fomel, 2007)

$$\hat{\mathbf{m}} = [\mathbf{I} + \mathbf{S} (\mathbf{L}^T \mathbf{L} - \mathbf{I})]^{-1} \mathbf{S} \mathbf{L}^T \mathbf{d} \quad (3.1)$$

where $\hat{\mathbf{m}}$ is a vector of model parameters; \mathbf{S} is the shaping operator; \mathbf{d} is the data; and \mathbf{L} and \mathbf{L}^T are the forward and adjoint operators, respectively. In interpolation problems, \mathbf{L} is forward interpolation (in the case of irregular sampling) or simple masking (in the case of missing-data interpolation on a regular grid). In 1-D, shaping in the Z -transform notation can be triangle smoothing (Claerbout, 1992)

$$T_n = \frac{1}{n^2} \left(\frac{1 - Z^n}{1 - Z} \right) \left(\frac{1 - Z^{-n}}{1 - Z^{-1}} \right) \quad (3.2)$$

for a given smoothing radius n . One can visualize this as a convolution of two box filters producing a weighting triangle with a neighborhood radius of n . Increasing n produces a smoother model. In 2-D, the shift operator Z translates into shifts of traces along local slope. $1 - Z$ corresponds to PWD (which can be thought of as a differentiation) while its inverse operator $\frac{1}{1-Z} = 1 + Z + Z^2 + \dots + Z^n$ corresponds to PWC (similar to integration).

INTERPOLATION TESTS

Interpolation is a simple example of a geophysical inverse problem (Claerbout, 2014). The two prerequisites for local plane-wave interpolation are simply the sparse data that are to be interpolated and the structure to which the reconstruction is shaped. In the following examples, I start with a seismic image and find the its local slope. I apply a mask to the image, leaving behind only a few nonzero traces. Following Clapp et al. (1998, 2004), I call these traces “wells” as a reference to the applicability of this method to well log data that might be desired everywhere but only provided in certain locations. Thus, the two inputs are the wells (to be interpolated) and the dip field (giving the direction of interpolation). By comparing the reconstruction to the original (non-sparse) data, I quantify the quality of the interpolation by measuring the model error.

2-D synthetic test

The quarterdome (Qdome) 3-D seismic image was created by Claerbout (1993). This model has been used for previous interpolation tests including those using both local plane-wave prediction filters (Fomel, 1999) and steering filters (Clapp et al., 1998; Clapp, 2000). The model and corresponding dip field are displayed in Figure 3.1 along with the decimated well data and local slope calculation. In order to demonstrate the local properties of PWS, its impulse response is shown along with those for PWD and PWC. Adding spikes to 50 random locations in the image and applying the operators produces the anisotropic response aligned with the local slope. A plot of the convergence rates is given in Figure 3.3. PWS converges in far fewer iterations — 6 as compared to the 55 required by PWD and 28 of PWC. By applying 2-D

interpolation with PWD, PWC, and PWS; I show a side-by-side comparison of the three methods after 60 iterations in Figure 3.4. All interpolation schemes produce similar results. The error sections — Figures 3.4(b), 3.4(d), and 3.4(f) — indicate comparable accuracy as well.

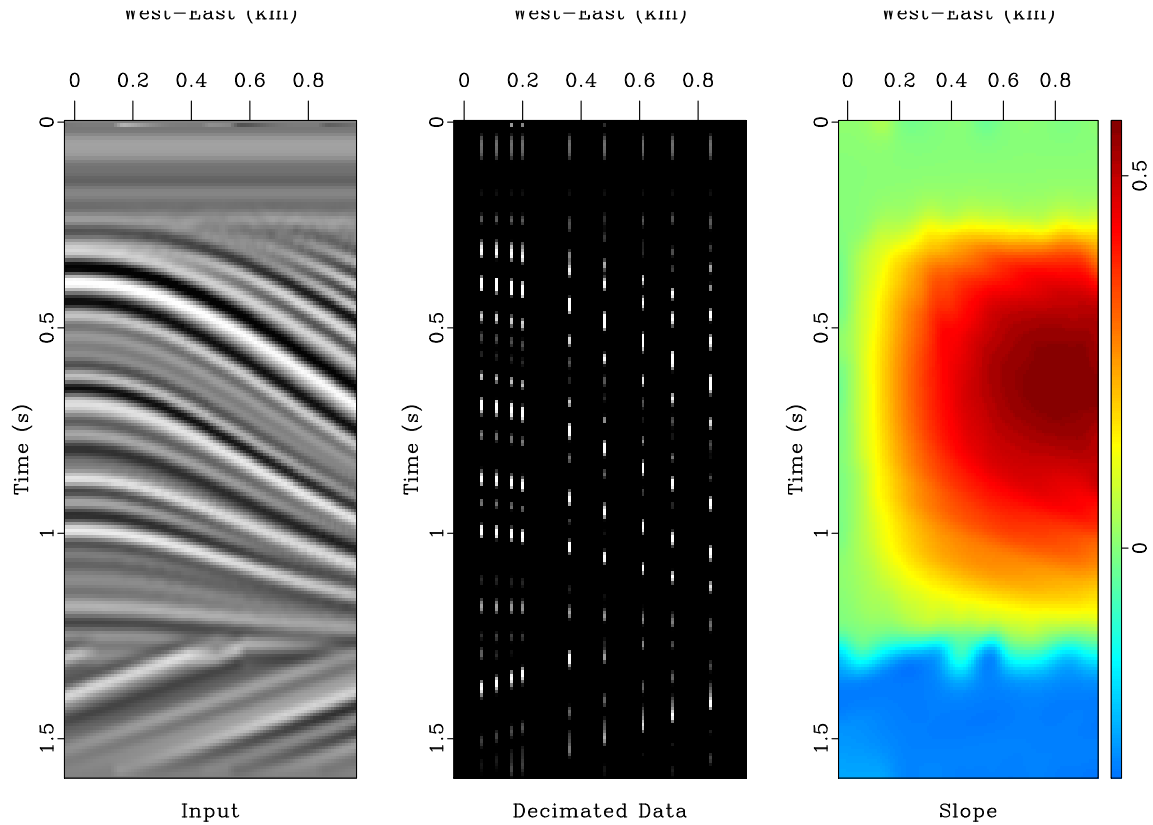


Figure 3.1: Synthetic example reproduced from Clapp et al. (2004). A 2-D slice of the quarterdome — Qdome — synthetic seismic image is given in (a) from which (b) the decimated data — wells — and (c) the dip field are derived. The nine traces were preserved in the application of the mask to produce the wells, and (c) is found by taking the local slope. `ch03-pws/qdome q-reflectors2`

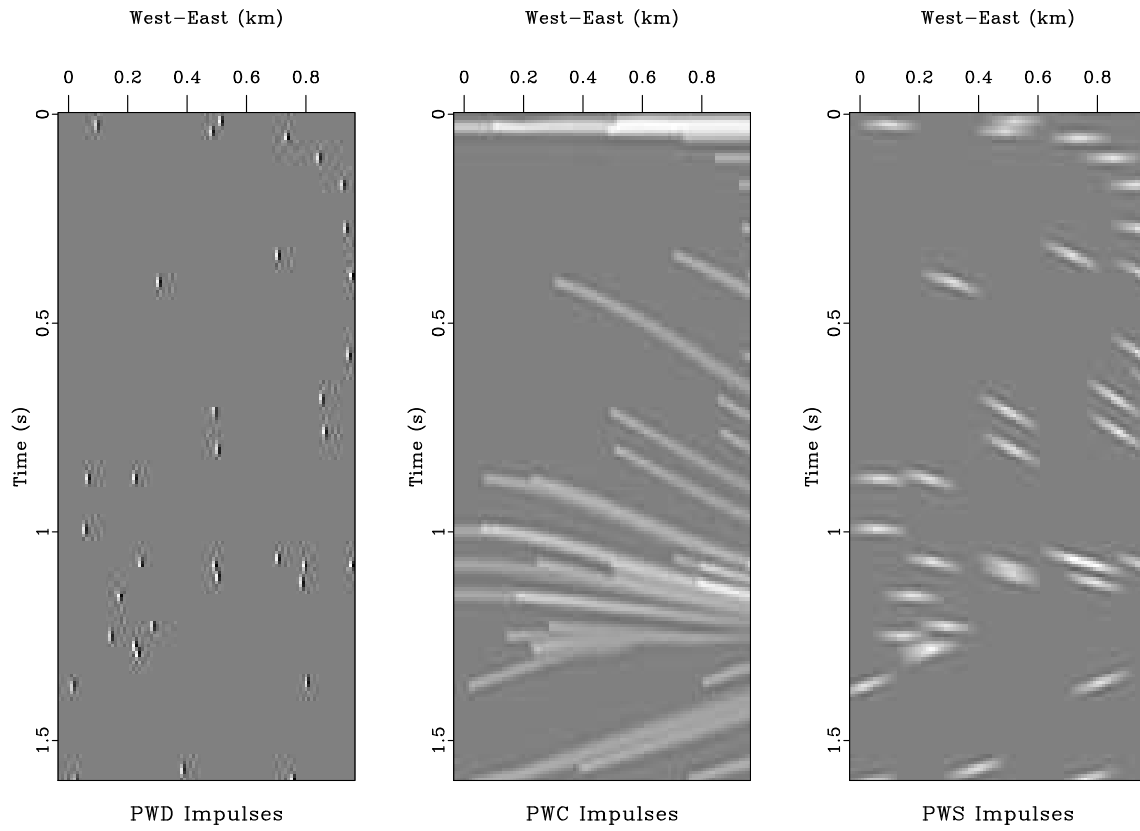


Figure 3.2: 2-D impulse responses. 50 spikes are placed randomly through the Qdome model and hit with the operators of (a) PWD, (b) PWC, and (c) PWS.
ch03-pws/qdome q-impulses

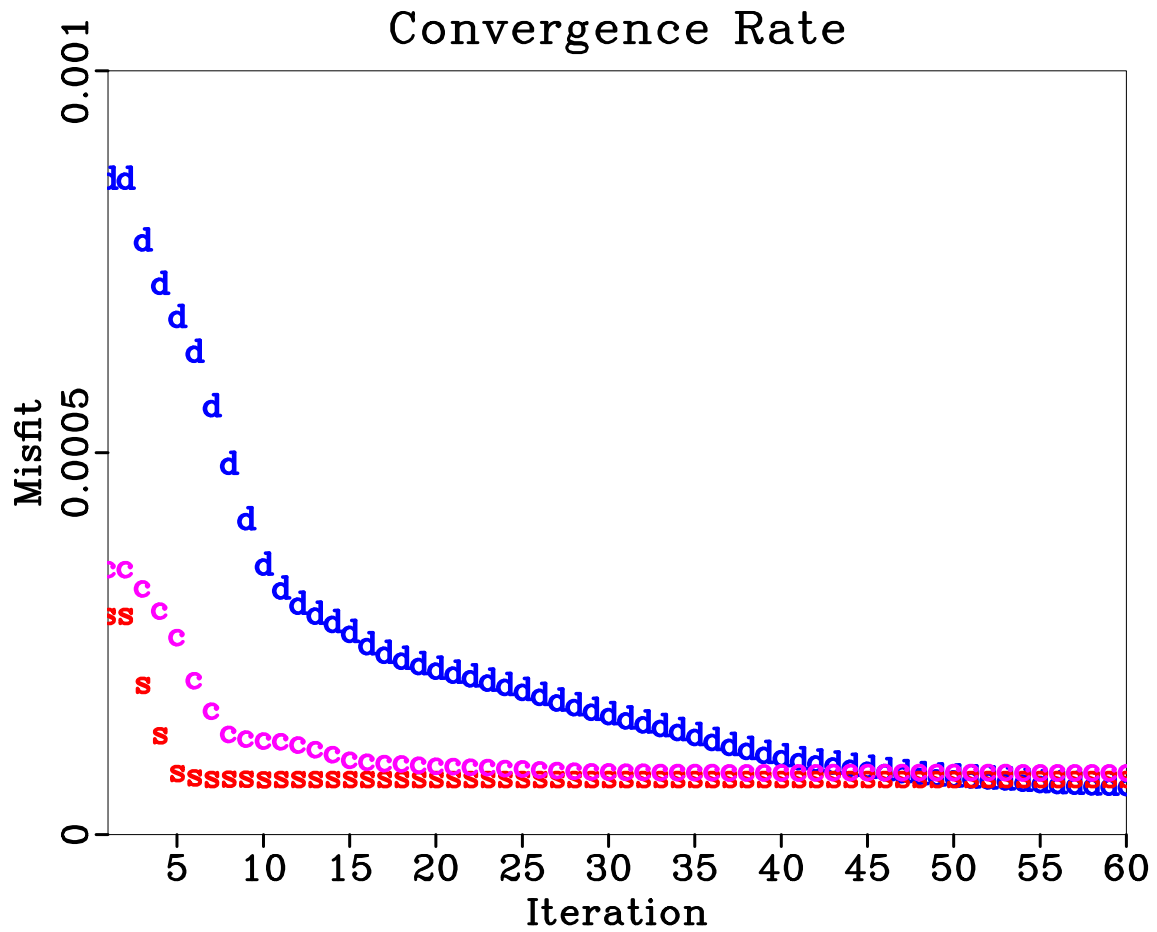


Figure 3.3: Convergence rate for 2-D synthetic example. This plot shows a comparison of the model error (2-norm) versus iteration number. The points denoted with “s” are derived from interpolation using PWS. The symbols “d” and “c” correspond to the same calculation using PWD and PWC, respectively.

ch03-pws/qdome q-Matrix1Comparison

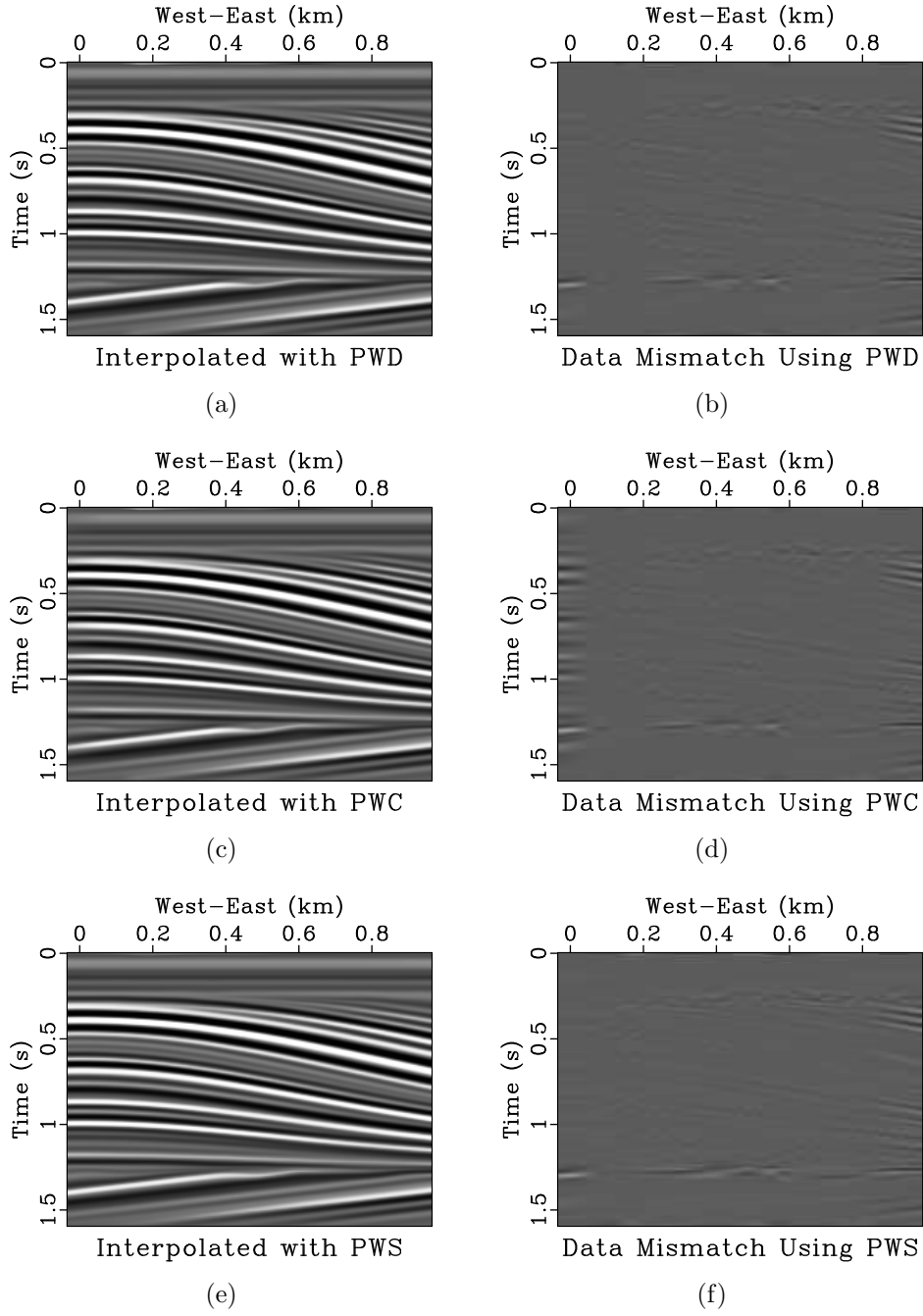


Figure 3.4: Reconstruction of 2-D synthetic data with interpolation from (a) plane-wave destruction, (c) plane-wave construction, and (e) plane-wave shaping. Parts (b), (d), and (f) correspond to the respective data misfit, computed with $\|d - d_i\|_2^2$ for the true solution d and reconstruction d_i at iteration i . Convergence was reached after 55, 28 and 6 iterations, respectively.

ch03-pws/qdome q-compa,q-compd,q-compb,q-compe,q-compc,q-compf

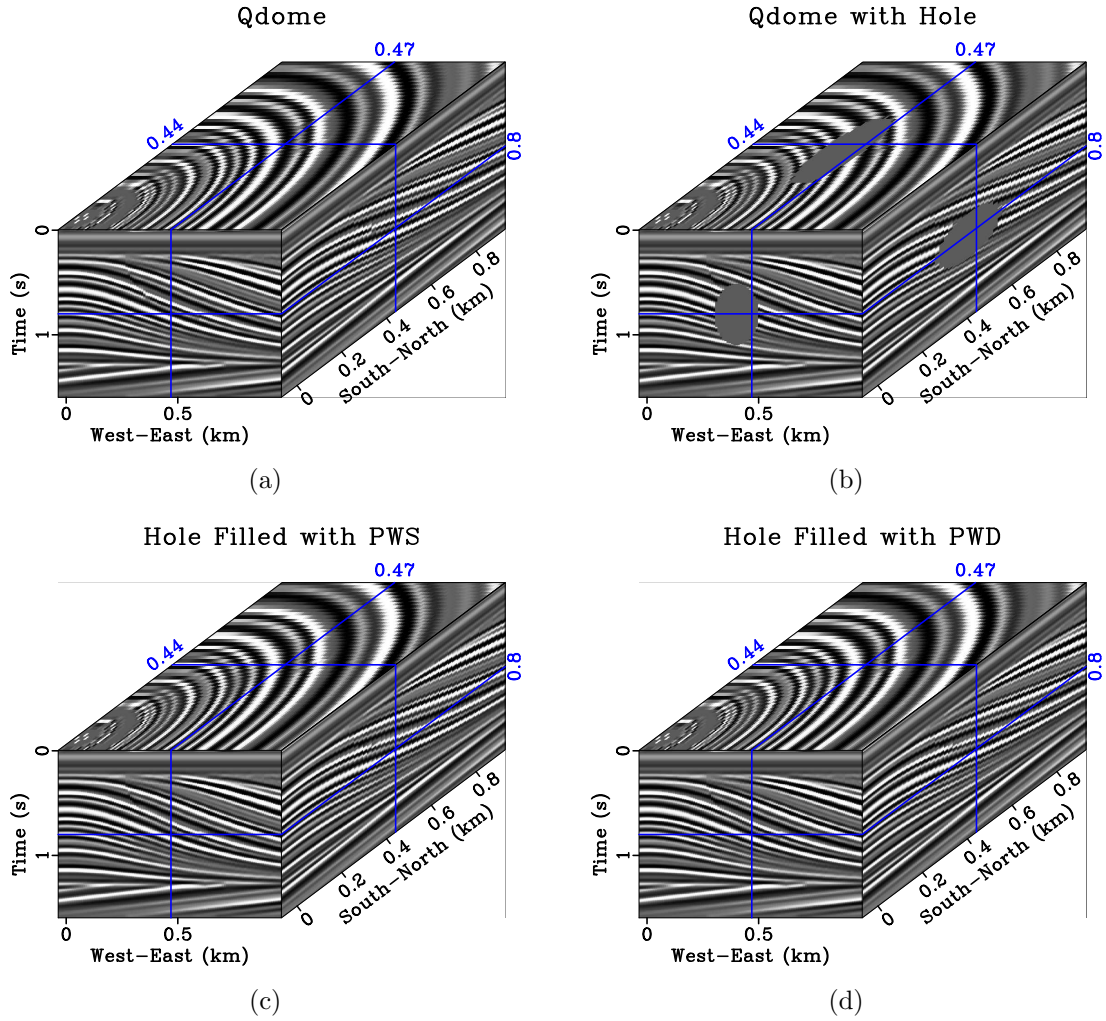


Figure 3.5: 3-D missing data fill. The original Qdome synthetic is shown in (a) and again in (b) with an ellipsoid-shaped hole of missing data. The reconstructions using PWS and PWD are shown in (c) and (d), respectively.

ch03-pws/qdome3 q3-orig,q3-hole,q3-PWS,q3-PWD

3-D synthetic test

In this experiment, I use the 3-D version of the Qdome seismic image and cut a large ellipsoid-shaped hole in the data. Using only this information, I can see how well applying 3-D PWS is able to reconstruct the original data without knowing the full original dip field. By finding the local slope of the masked image, PWS interpolation can then be applied. These local slopes are displayed in Figure 3.6 as the inline and cross-line components. The 3-D impulse response is shown in Figure 3.7 and shows the shaping of information to the synthetic geologic structure in 3-D. Figure 3.5 shows the data (a) originally, (b) with the mask applied, and (c) with reconstruction. The resulting interpolation accurately patches the hole. The only area where the result mildly deviates from the answer is adjacent to the fault. Here, PWS smooths over the fault to make it somewhat more continuous.

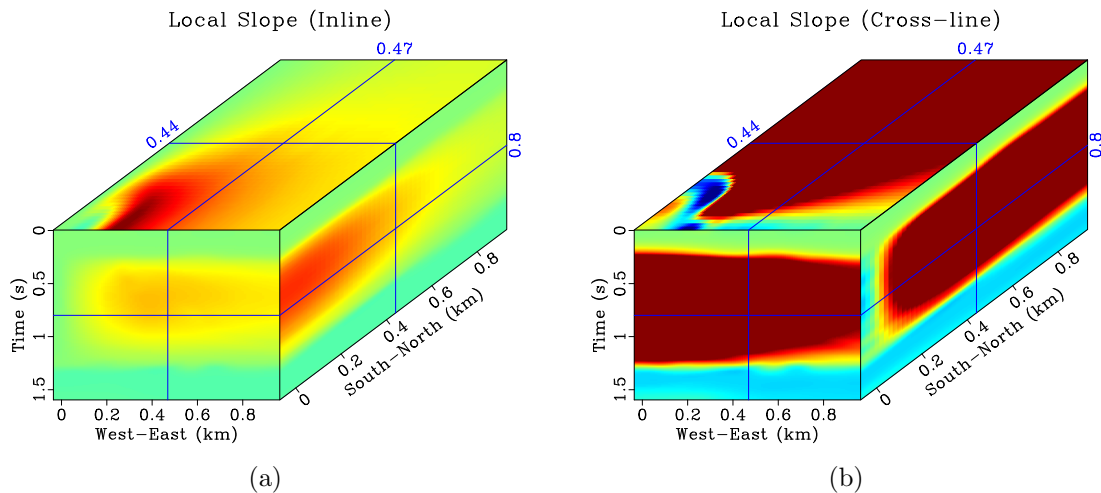


Figure 3.6: Dip field of 3-D Qdome image with ellipsoid-shaped hole with the (a) inline component and (b) cross-line component `ch03-pws/qdome3 idip-q3hole,xdip-q3hole`

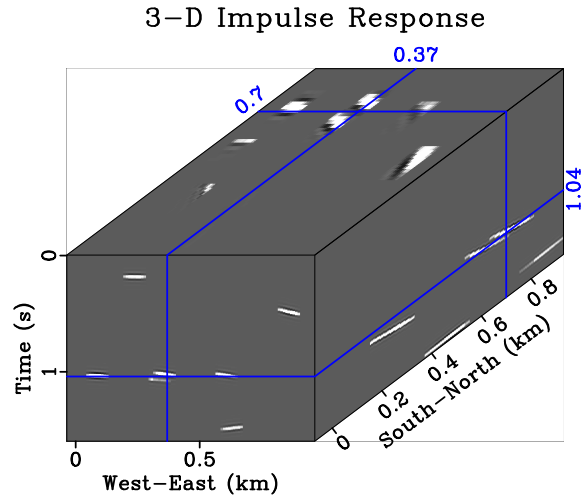


Figure 3.7: 3-D impulse response. 20 spikes are randomly placed in the 3-D qdome model. These peaks are smeared in a structure-guided fashion by 3-D PWS to produce this image. `ch03-pws/qdome3 q3-imp`

Field data test

The Parihaka data is a 3-D (full-angle stack, anisotropic, prestack time-migrated) seismic image from New Zealand provided for use by New Zealand Petroleum and Minerals. The data cube is shown in Figure 3.8(a). Similar to the synthetic test, I mask the data, Figure 3.8(b), and interpolate using PWS. The interpolation results are shown in Figure 3.8(c) with error section in 3.8(d). The residual was sufficiently low after only 4 iterations. Because this scheme amounts to some quantity of smoothing, the fault that propagates clearly in the original seismic image is now smeared. However, PWS continues to maintain the structural information of this fault's existence from the offset of beds.

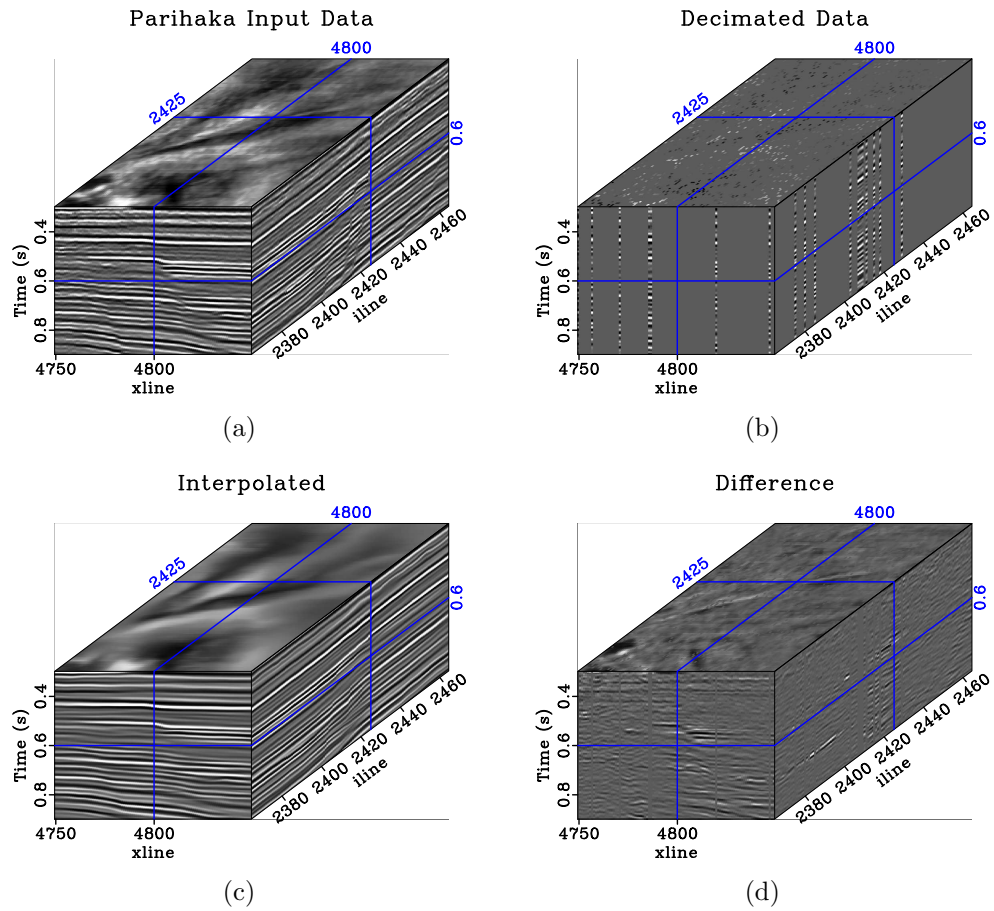


Figure 3.8: Field data interpolation example. The original data is depicted in (a) and a mask, shown in (b), is applied to heavily decimate the input to create a set of wells. (c) shows the interpolated result of PWS, and (d) is the difference between the reconstruction and the original. The smallest-scale features and noise are removed as a result of the smoothing. ch03-pws/parihaka p3-orig,p3-deci2,p3-shfill2,p3-sherr2

CONCLUSIONS

Plane-wave shaping (PWS) is a powerful tool for constraining the solutions to inverse problems that require conforming to a local plane-wave structure. The impulse responses in both 2-D and 3-D verify this image-guided nature. I demonstrate the effectiveness of PWS as an interpolation scheme using simple missing-data interpolation experiments on both field data and synthetic examples and show that the method converges to a low misfit in fewer iterations than alternative regularization schemes which use either PWD or PWC. The benefit of fast convergence comes from the fact that oftentimes large-scale geophysical inverse problems can afford only a small number of iterations. When stopping the inversion after only a small number of iterations, PWS appears to produce a more accurate estimation of model parameters than either PWD or PWC. PWS also has a more straightforward extension from 2-D to 3-D. These properties give PWS high potential for geophysical applications beyond simple interpolation.

Chapter 4

Data Interpolation Experiments

INTRODUCTION

When data are missing from a seismic survey, interpolation can attempt to fill the gaps with synthetic information. In this chapter, I apply plane-wave shaping (PWS) in three blind tests: the SeaBeam image, the Blast seismic dataset, and the P-cable marine seismic dataset. These experiments have not been deliberately decimated to produce the holes to be filled by an interpolation scheme like that of the previous experiments in Chapter 3. Instead, the datasets here all have missing data because of trouble with the data's acquisition, such as dealing with physical obstacles or equipment malfunction. The same tests are then conducted for other interpolation schemes: plane-wave destruction (PWD) and plane-wave construction (PWC). In this chapter, I also investigate the parameter sensitivity and computational cost of PWS and build random realizations of a reconstruction which capture textural information comparing PWS and prediction-error filters (PEFs).

SEABEAM BENCHMARK DATA

The SeaBeam image, named after the instrument used to gather the data, is a map of the water bottom along a seafloor spreading center. The SeaBeam image, presented by Claerbout and Fomel (2014) and shown in Figure 4.1, is marked by its irregular and sparse coverage, making it a great 2-D example for testing different

interpolation schemes. This image specifically has very little information to be used in constraining a solution near the upper and lower right corners of the survey. Tasking PWS with interpolating this image pushes the algorithm to its limits, giving valuable insight about its behavior and exposing possible limitations. For comparison, I test the other interpolation schemes of PWD and PWC as well.

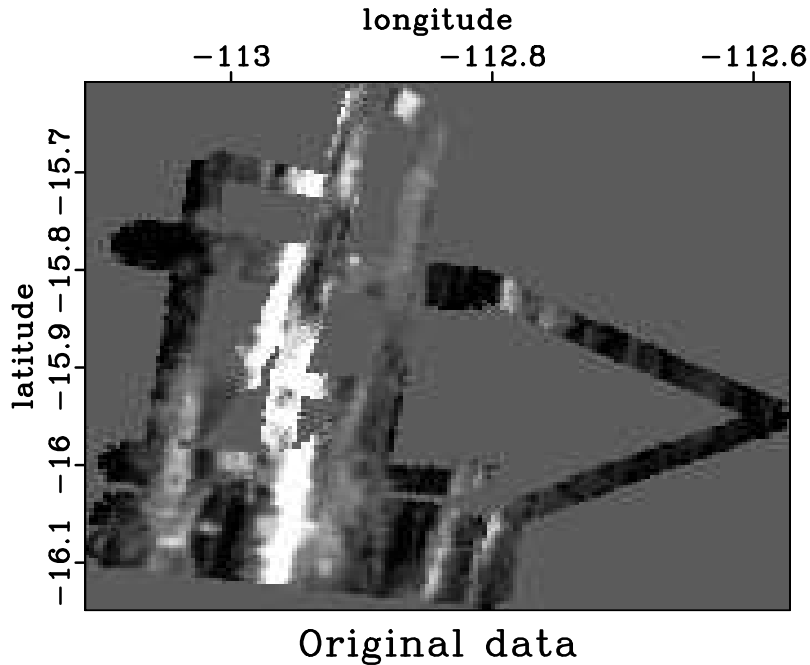


Figure 4.1: SeaBeam data `ch04-p-cable/seab binseab`

To begin, a mask (shown in Figure 4.2) is extracted from the data to be used with the interpolation techniques in order to preserve the original data by reinstating it after any possible corruption (e.g., smoothing). The plane-wave schemes work using information derived from the local slope. This dip field is calculated in Figure 4.3. Even with smoothing, this image looks blotchy in the areas where information concentration is highest and smeared to the top and right. With these prerequisites, PWS, PWD, and PWC are all applied.

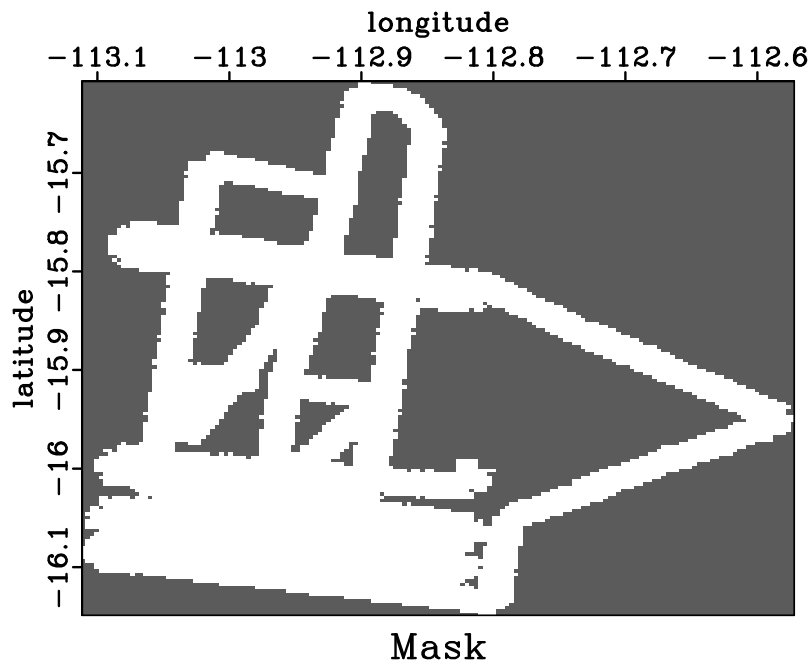


Figure 4.2: SeaBeam data mask `ch04-p-cable/seab mask`

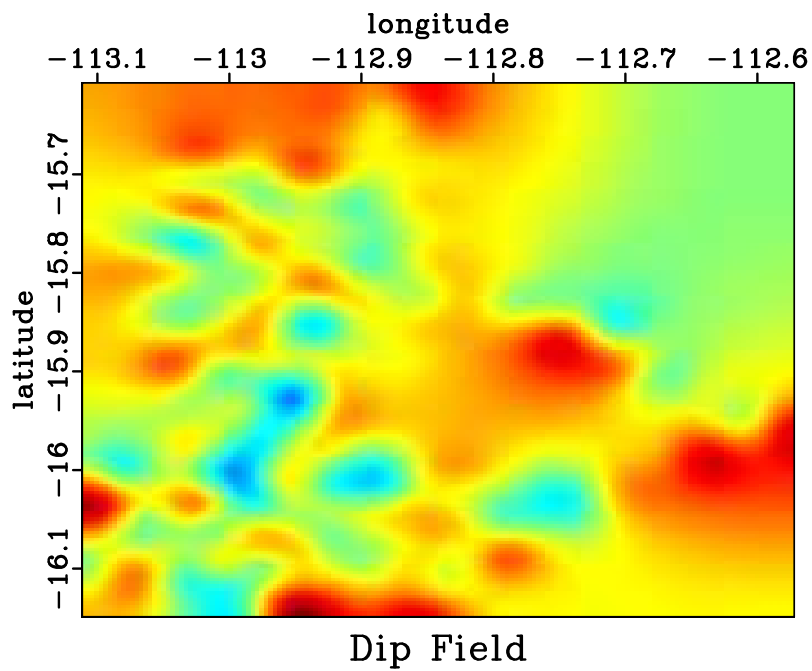


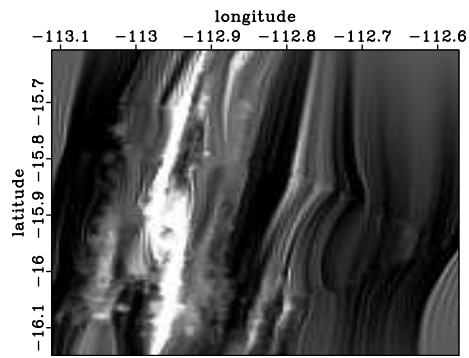
Figure 4.3: Estimated local slope of the SeaBeam data `ch04-p-cable/seab dip`

SeaBeam Results

For these tests, padding the sides of the data in all dimensions by 35 zeroed traces was sufficient to remove the edge-effects of applying the filters. The reconstructions produced from interpolation using PWD, PWC, and PWS (with smoothing radius of 70) are shown in Figure 4.4. Notice the manifestation of original data's holes in the dip field (Figure 4.3). The plane wave techniques exhibit the same smearing effect that was observed in the local slope calculation and struggle in these same areas. They cannot operate effectively in large empty spaces because of the lack of information which it would use to constrain a solution. As a result, the algorithms behaves undesirably in these regions. In general, the plane-wave techniques all perform well and produce comparable results. Visibly, PWD and PWC experience a high-wavenumber noise, notably in areas such as the triangular cavity and the lower right corner of the image. PWS does not experience this phenomenon because of its smoothing nature. As a result, the amplitudes that PWS produces are more consistent in their plausibility than with the other techniques.

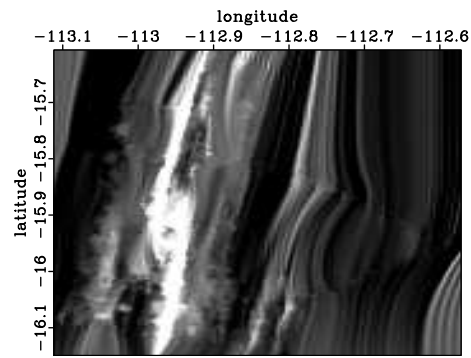
PWS PARAMETER INVESTIGATION

In this section, I explore the sensitivity of the key parameters which are used in PWS. The first is the only required parameter, the smoothing radius. It governs how many adjacent traces away to take information from when producing the interpolated dataset for a given location at any iteration. I expected that the time per iteration grows linearly with increased smoothing radius. To test this, at several smoothing radii, the total duration for 100 iterations of PWS was recorded for the SeaBeam dataset. These data are presented in Table 4.1. Notice that the total time and time



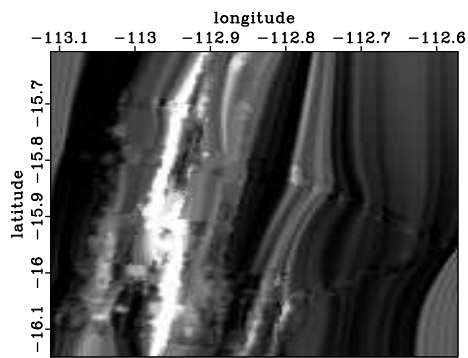
Interpolation using pwd

(a)



Interpolation using pwc

(b)



PWS with $r=70$

(c)

Figure 4.4: SeaBeam reconstruction using (a) PWD, (b) PWC, and (c) PWS
 ch04-p-cable/seab real-pwd,real-pwc,real-pws-ns70pad35

per iteration grow linearly with increasing radius n_r , showing that the computation time is $\mathcal{O}(n_r)$ concerning only the radius.

Table 4.1: Computational time dependence on smoothing radius for SeaBeam data

Smoothing Radius n_r [samples]	Total Time [s] ± 1 [s]	Time/Iteration [s]
1	2	2
5	10	2
10	20	2
20	39	2
30	57	1.9
40	74	1.9
50	91	1.8

When working with irregular data, choosing a smoothing radius can seem non-obvious. One of the benefits of using PWS is that the interpolation is not incredibly sensitive to the choice of radius. A good rule of thumb is to choose the smoothing radius to be about the size of the hole to be filled. In this case, the SeaBeam data has a sizable hole in the middle, approximately 70 traces at its largest separation. With this reasoning, I chose the smoothing radius to be 70 for the final comparison between the tests.

If the data is sparsely sampled (such as in the case of SeaBeam), the next item to address is the size of the padding that will be appended to the edges in all dimensions. This padding is often necessary to remove unseemly artifacts induced by the edges of the image. A reasonable estimate for this value is half of the smoothing radius. In the instance above, 35 became the padding size. If the padding is too small or nonexistent, artifacts along the edges can be produced along with spurious amplitudes. Making the padding too large does not adversely affect the accuracy of the final reconstruction, but it does increase the computation time by making the problem

size larger. The compromise comes in finding a padding size large enough to remove artifacts without becoming too large to waste valuable computational resources.

To test both of these heuristic principles and to gather evidence to support them, I examine a range of radii — specifically 30, 40, 50, 60, 70, and 80 — for a range of padding values — specifically 1, 10, 20, 35, 50, and 100. In this experiment, the number of PWS iterations is set constant to 5. The interpolated data which most resemble the original data are considered to have the greatest success.

The results are shown in Figures 4.5–4.10. The result of not padding is emulated with a pad of 1 point in Figure 4.5. This collection of images shows strong edge effects that occur primarily in the lower-right of each of the panels. Another negative consequence is produced by choosing too small of a smoothing radius for too few iterations; the interpolation fades out before covering the original area of missing data. The interpolation simply cannot handle far-reaching gaps in the number of iterations that it was provided. In the second panel of Figure 4.6 (corresponding to a smoothing radius of 40), the aforementioned amplitude anomaly, which is artificially introduced with a gap size being too small, is easily noticeable. Even without these artifacts, the interpolation does a poor job when the padding is far less than the radius, as seen the rightmost panel of Figure 4.7 (smoothing radius of 80). Choosing a padding of 35 (Figure 4.6) produces well-behaved, believable results for smoothing radii 60, 70, and 80. Good reconstructions are also made for the larger smoothing radii for large values of padding of 50 and 100 (Figure 4.9 and Figure 4.10). Over this range in parameter space, very few changes occur concerning the accuracy of the final reconstruction. With a very large padding value, the interpolation takes more time to do very little. Thus, the general rule holds: choose a padding value of approximately half of the size of the smoothing radius, erring on the larger side.

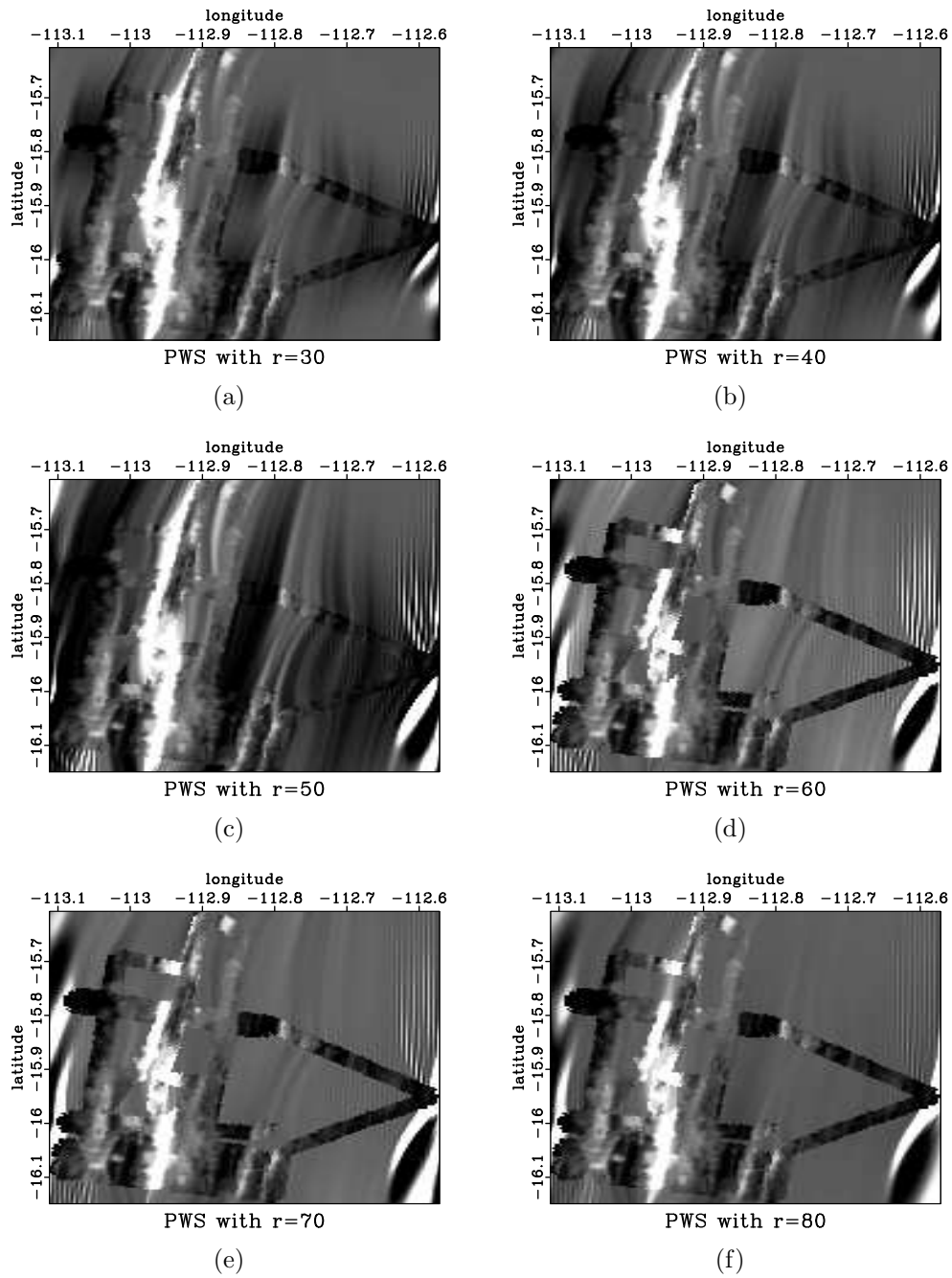


Figure 4.5: SeaBeam interpolated image using PWS with a spatial padding of 1 on all sides and smoothing radii (r) of 30, 40, 50, 60, 70, and 80, respectively.

ch04-p-cable/seab rsn30p1,rsn40p1,rsn50p1,rsn60p1,rsn70p1,rsn80p1

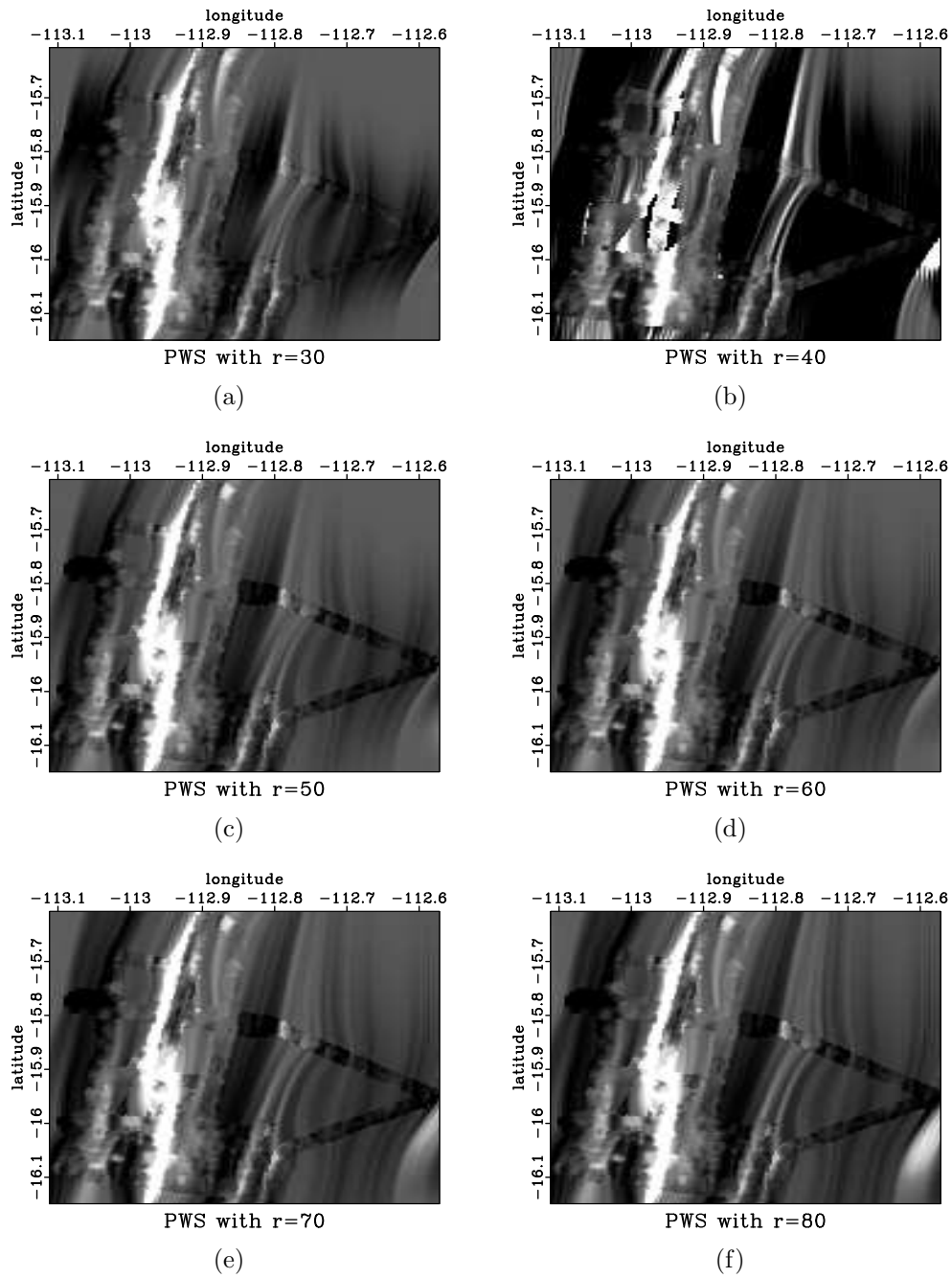


Figure 4.6: SeaBeam interpolated image using PWS with a spatial padding of 10 on all sides and smoothing radii (r) of 30, 40, 50, 60, 70, and 80, respectively.

ch04-p-cable/seab rsn30p10,rsn40p10,rsn50p10,rsn60p10,rsn70p10,rsn80p10

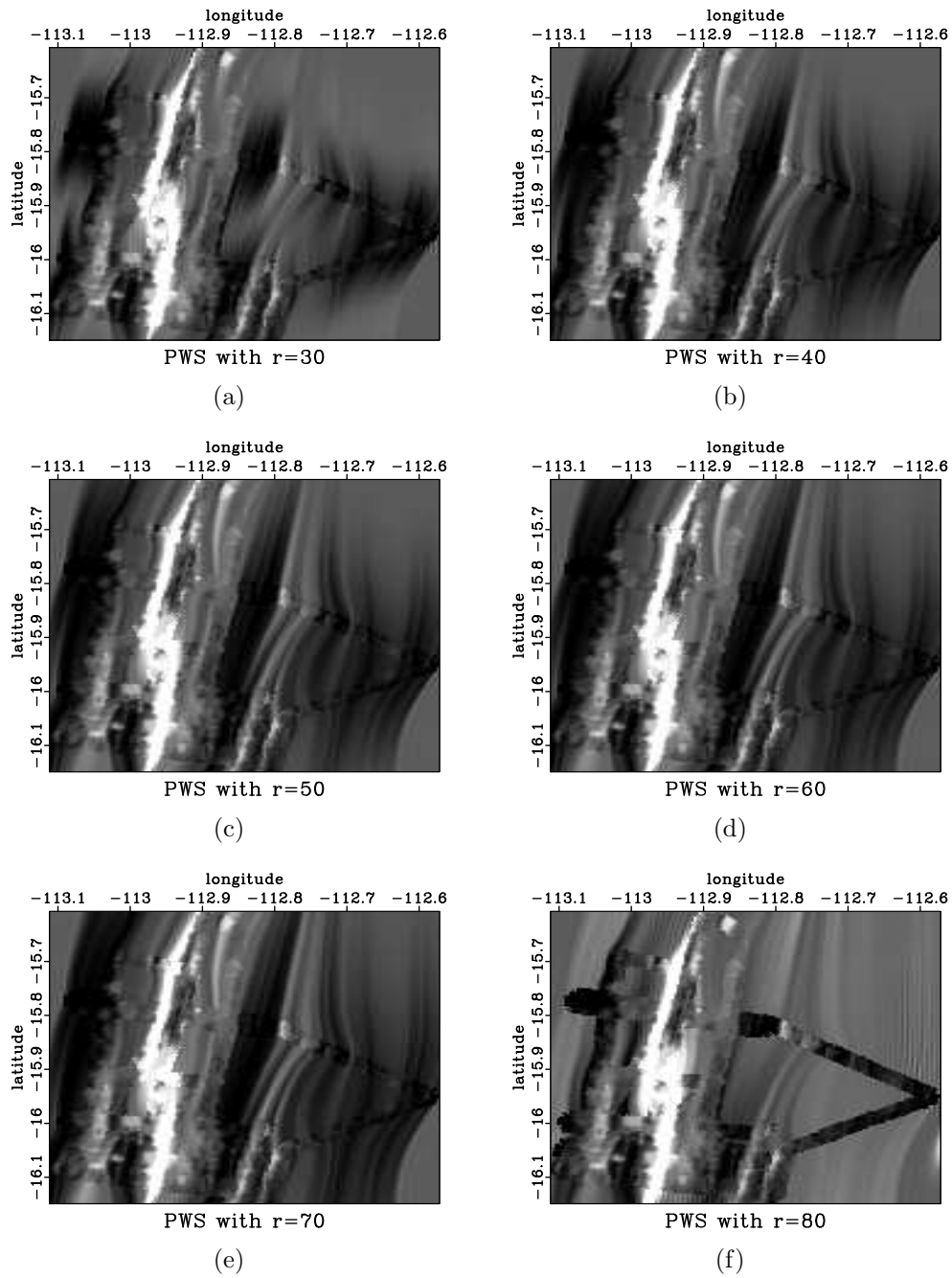


Figure 4.7: SeaBeam interpolated image using PWS with a spatial padding of 20 on all sides and smoothing radii (r) of 30, 40, 50, 60, 70, and 80, respectively.

ch04-p-cable/seab rsn30p20,rsn40p20,rsn50p20,rsn60p20,rsn70p20,rsn80p20

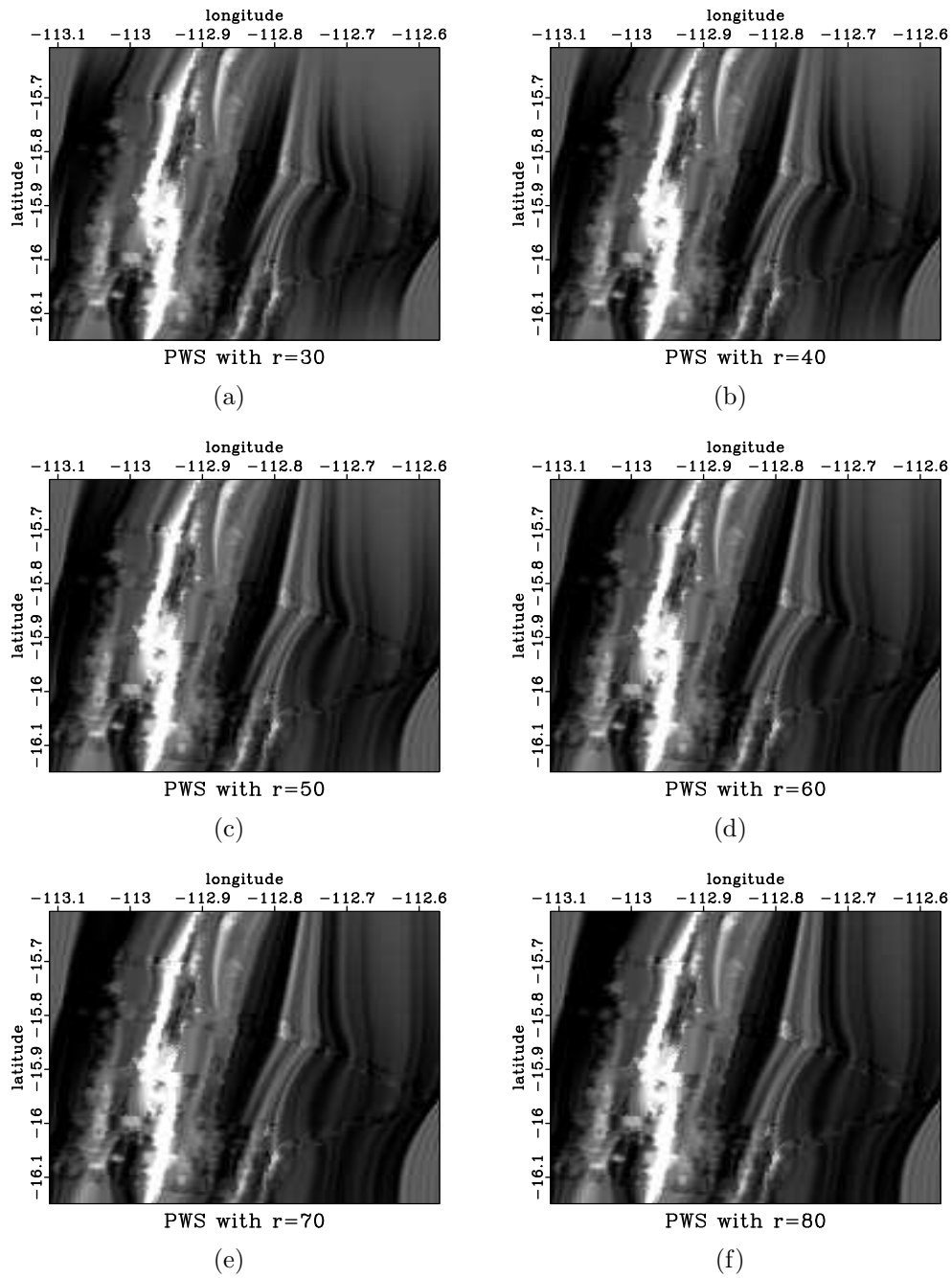


Figure 4.8: SeaBeam interpolated image using PWS with a spatial padding of 35 on all sides and smoothing radii (r) of 30, 40, 50, 60, 70, and 80, respectively.

ch04-p-cable/seab rsn30p35,rsn40p35,rsn50p35,rsn60p35,rsn70p35,rsn80p35

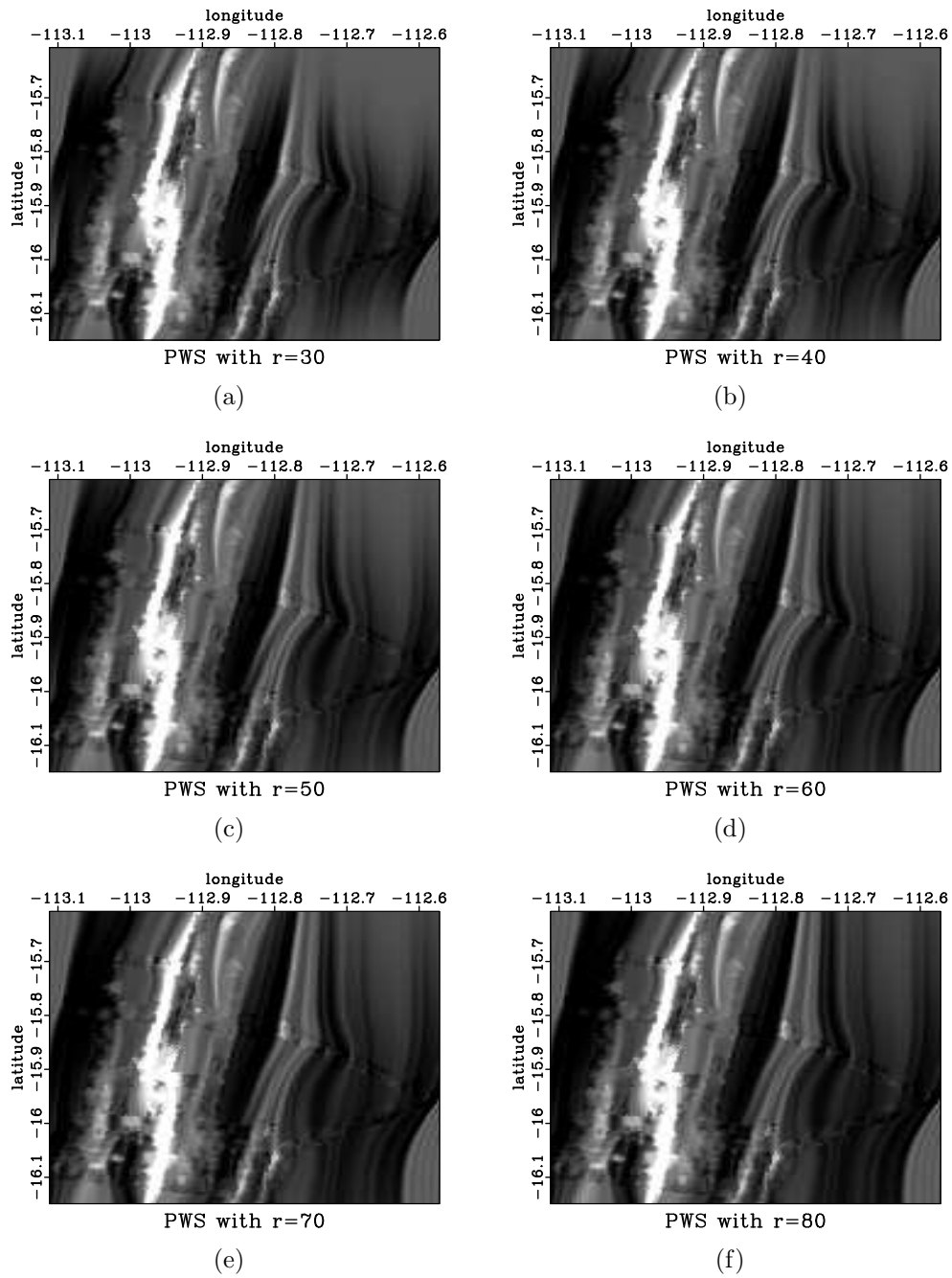


Figure 4.9: SeaBeam interpolated image using PWS with a spatial padding of 50 on all sides and smoothing radii (r) of 30, 40, 50, 60, 70, and 80, respectively.

ch04-p-cable/seab rsn30p50,rsn40p50,rsn50p50,rsn60p50,rsn70p50,rsn80p50

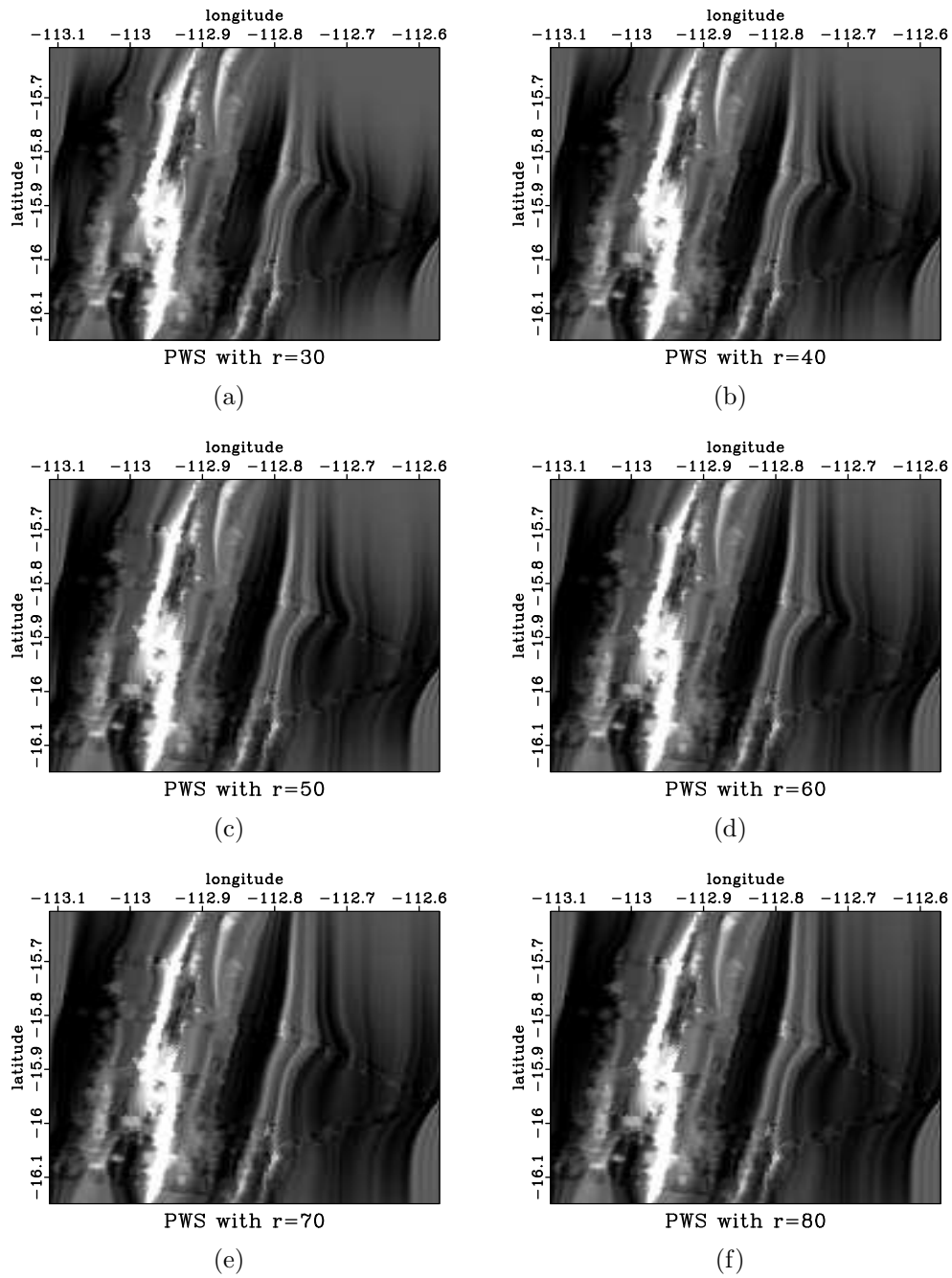


Figure 4.10: SeaBeam interpolated image using PWS with a spatial padding of 100 on all sides and smoothing radii (r) of 30, 40, 50, 60, 70, and 80, respectively.

ch04-p-cable/seab rsn30p100,rsn40p100,rsn50p100,rsn60p100,rsn70p100,rsn80p100

If the padding became too large, the computational cost would increase. The total time increases linearly with data size. This effect is reproduced by running the experiment several times with different data sizes and recording the time to completion. I do this for 4 iterations of PWS with constant smoothing radius. The results of this test are presented in Figure 4.11. Indeed, the computational cost is simply linear in data size.

Putting these findings together, I verify that the computational cost of PWS is linear and can be expressed as $\mathcal{O}(N_i N_r N)$ for N_i number of iterations, N_r size of smoothing radius, and N number of data points. If both N_i and N_r are small and independent of N , the cost is linear.

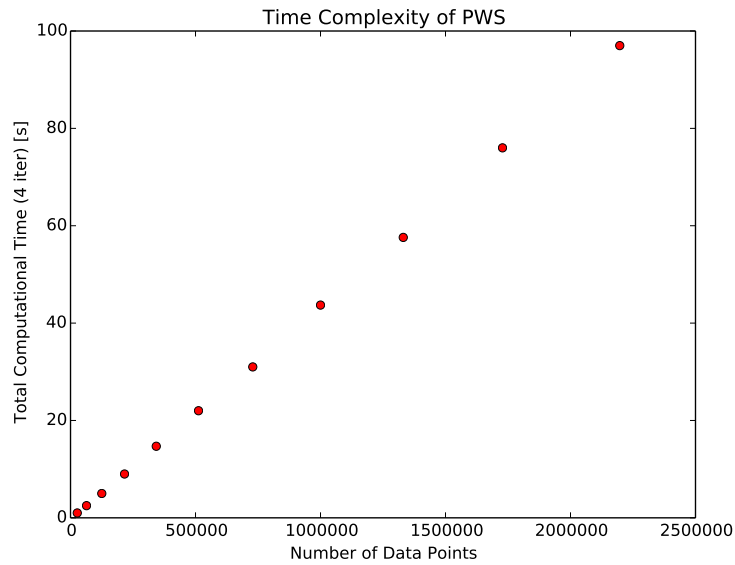


Figure 4.11: Graph of computation time versus input data size for PWS
ch04-p-cable/seab time

Random Realizations

The reconstruction produced by PWS appears smooth, as expected, from the insight gained by the algorithm's Z-transform notation as a triangle smoother. The problem associated with this behavior is that the original data does not match the same smoothness as the reconstructed model. A way to compensate for this is to introduce random noise into the process of selecting a model. In doing so, we can inherently introduce artificial information into the end result which is dependent on those random numbers, but the final product can better match the character of the initial data, which will look more realistic. I complete this process and using PWS and prediction-error filters (PEF). The strategy is as follows:

1. Apply PWD to example model
2. Measure variance
3. Make random noise \mathbf{r} of the same variance
4. Build initial model by applying PWC: $\mathbf{m}_0 = \mathbf{D}^{-1}\mathbf{r}$
5. Change data: $\mathbf{d}_0 = \mathbf{d} - \mathbf{K}\mathbf{m}_0$
6. Interpolate \mathbf{d}_0 to get $\hat{\mathbf{m}}$ using an appropriate method
7. $\mathbf{m} = \hat{\mathbf{m}} + \mathbf{m}_0$

In the first step, I take the reconstruction using PWS as an example model. By applying PWD to this image (shown in Figure 4.12) the destruction residual is produced. The variance of these data is $8.4 \cdot 10^{-4}$. Using this information of the variance, I synthesize pseudo-random Gaussian white noise with several seeds using

the same variance. Using this noise, I apply PWC (the inverse of PWD) to retrieve a new model, \mathbf{m}_0 , which, in some sense, is an extracted random texture of the original data. This texture is depicted in Figure 4.13. Because it was derived from Gaussian white noise, the values in this image can change, but visually the texture remains unchanged. The altered data \mathbf{d}_0 is then formed by subtracting the masked texture from the original data. This perturbed data then gets interpolated using plane-wave shaping, in this case with a smoothing radius of 70 and padding on all sides of 35. The result of this process, $\hat{\mathbf{m}}$, yet is not the end result. The final reconstructed image, \mathbf{m} , is a sum of $\hat{\mathbf{m}}$ and \mathbf{m}_0 . Four realizations of this are provided in Figures 4.14(c)–4.14(f) alongside the original data (Figure 4.14(a)) and the model found using PWS without any noise addition (Figure 4.14(b)).

Although the realizations are a bit different, they all share the same texture present in the original data. Averaging a large number of these realizations would yield the unperturbed, original PWS reconstruction of Figure 4.14(b).

Similarly prediction-error filters (PEFs) can be used to create random realizations of the reconstruction. For an example seed of white noise, the extracted pattern is noticeably striped and shown in Figure 4.15, and the spectrum of the PEF is found and provided in Figure 4.16. Notice the clustering of high amplitudes associated with low wavenumbers in the x- and y-directions (i.e., the longitudinal and latitudinal directions, respectively).

For four seed values, I construct PEFs and apply them to the data. This action is done both with and without preconditioning. Figure 4.17 shows the interpolation results without using preconditioning. Even with a sufficiently high number of iterations (500 in this case) the PEF-based interpolation fails to provide entirely

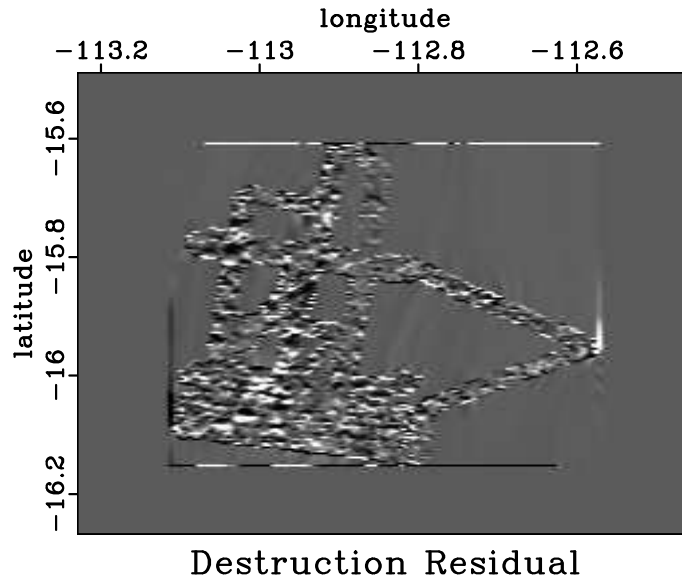
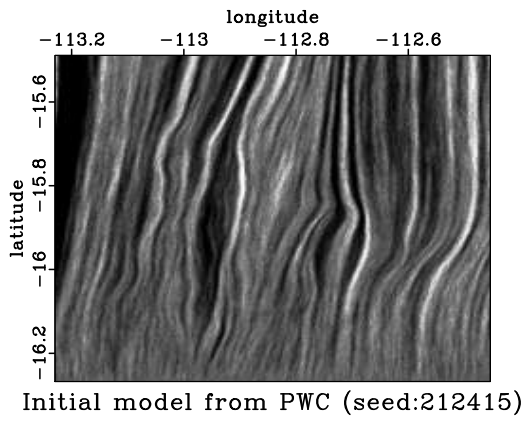


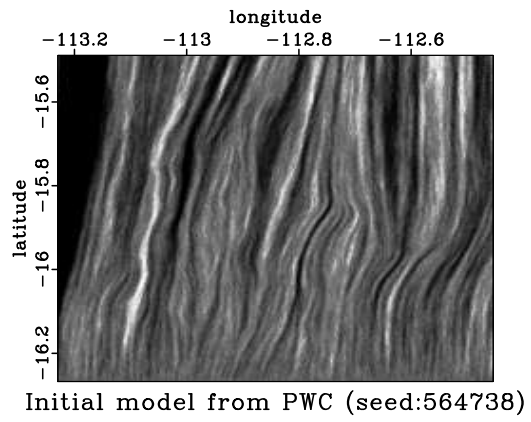
Figure 4.12: Destruction residual of PWS reconstruction
 ch04-p-cable/seab sb-pws4sfattr

realistic results. Using preconditioning (displayed in Figure 4.18) does not improve the behavior. The reconstructions using PEFs generally leave the largest holes only mildly affected. The acquisition footprint remains although some of the very small gaps are successfully compensated.

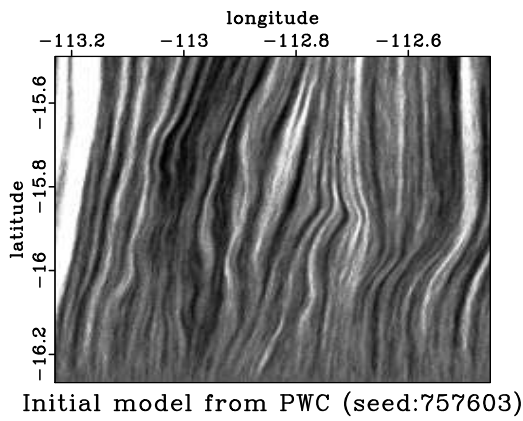
The PWS realizations are far better at filling the largest gaps in the data in a plausible way than the PEF-based method. The comparable amplitudes inside and outside the mask and preserved texture are credited as the winning factors. Although these random realizations can be visually appealing, they introduce features in the data that might be easily misinterpreted as geological. For this reason, I do not use them for the remainder of the tests.



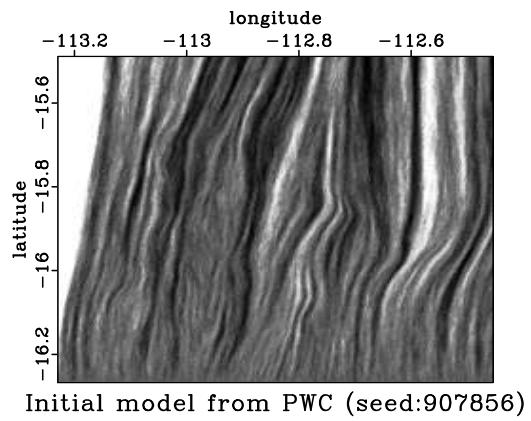
(a)



(b)



(c)



(d)

Figure 4.13: Initial model created by PWC
 ch04-p-cable/seab sbs-s2m0,sbs-s5m0,sbs-s7m0,sbs-s9m0

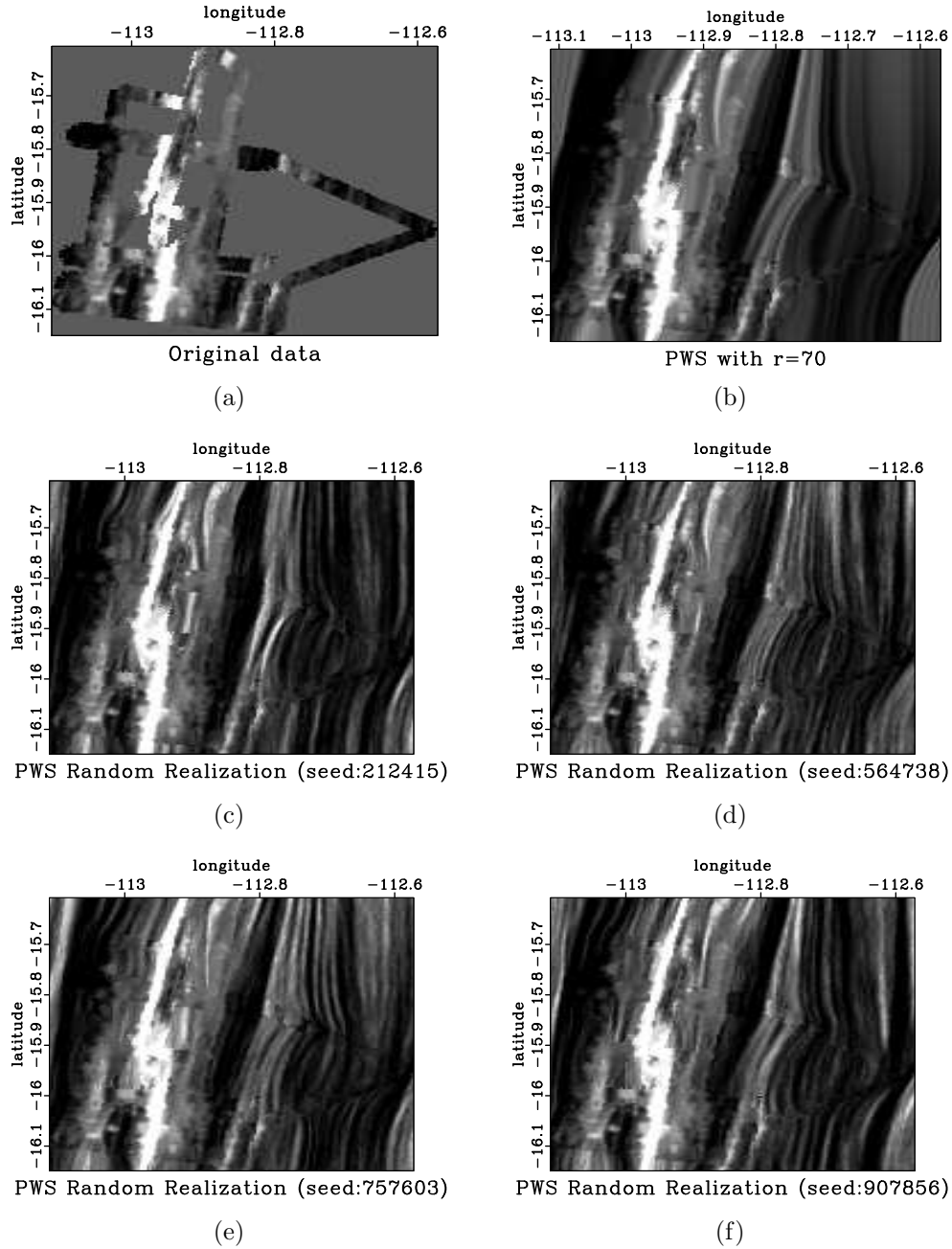
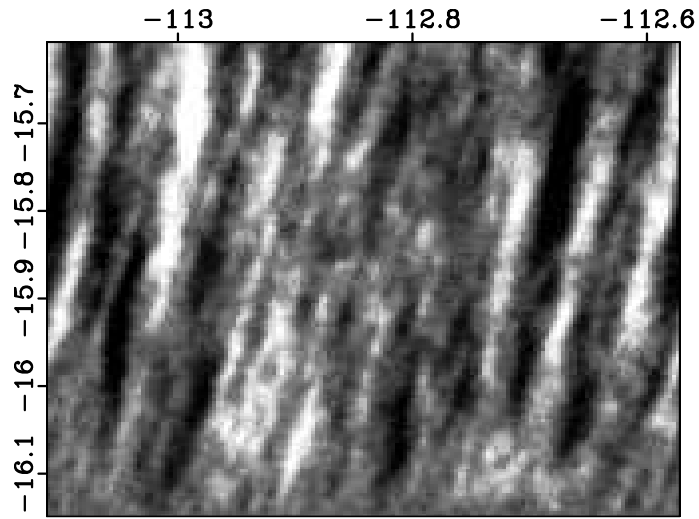
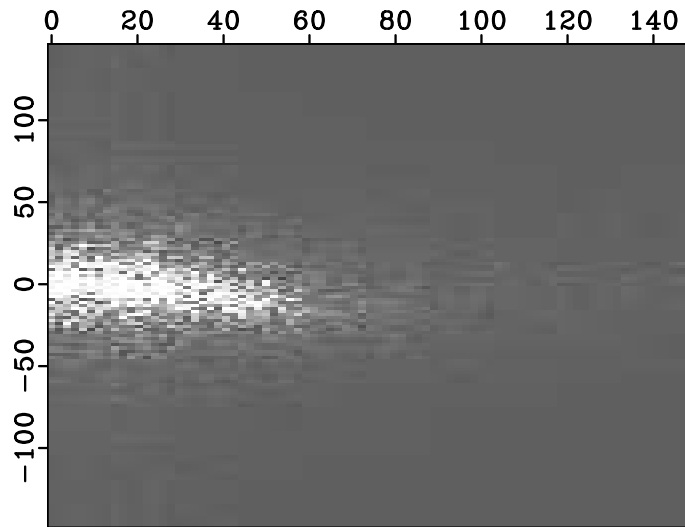


Figure 4.14: Depiction of (a) Original SeaBeam data, (b) PWS interpolation using smoothing radius of 70 and a padding size of 35 on all edges, and (c)–(f) random realizations of PWD with different seeds `ch04-p-cable/seab bin,real-pws-ns70pad35,sbs-s2m,sbs-s5m,sbs-s7m,sbs-s9m`



REF Pattern (seed:212415)

Figure 4.15: Example REF Pattern `ch04-p-cable/seab sb-pef-212415rand`



PEF Spectrum (seed:212415)

Figure 4.16: Example Spectrum of PEF `ch04-p-cable/seab sb-pef-212415frand`

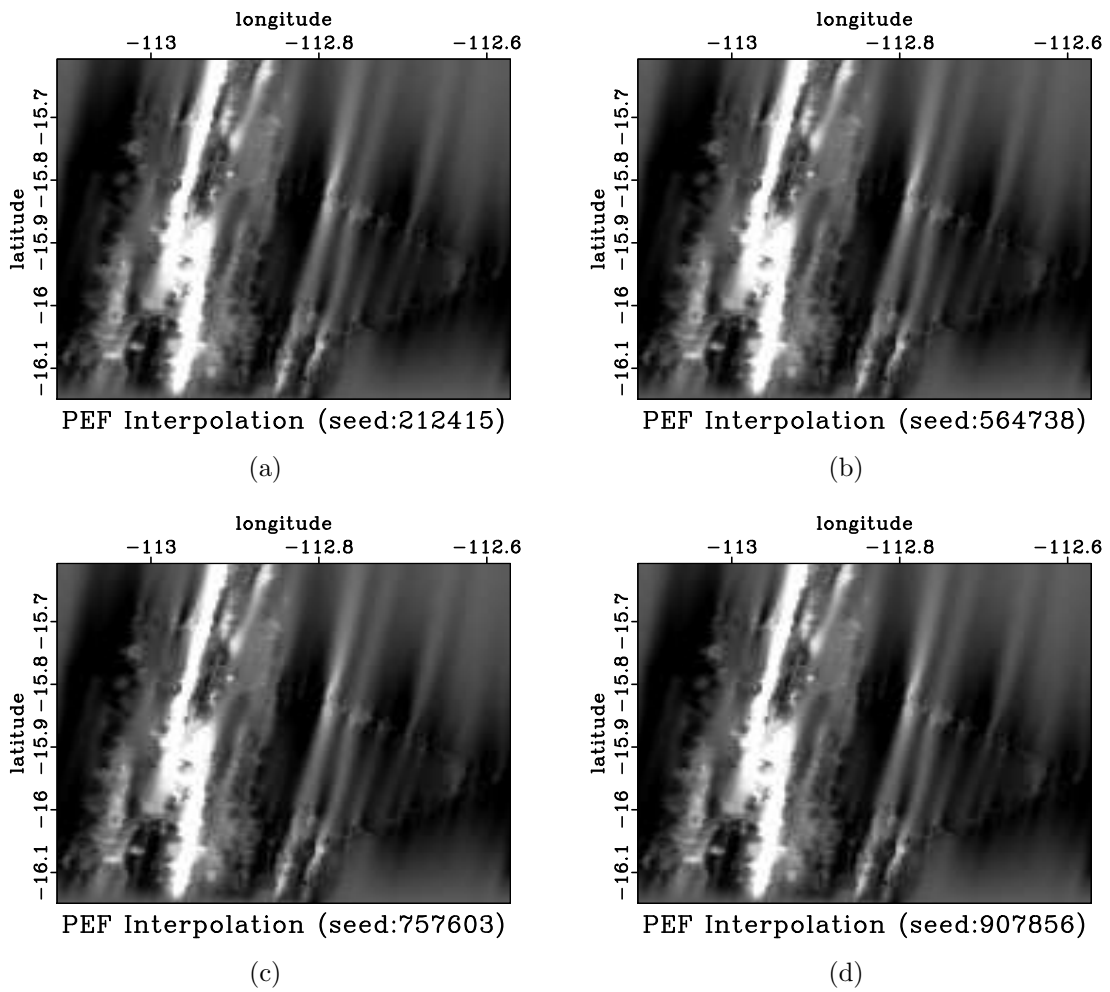


Figure 4.17: Reconstructions from the adjusted data using PEF-based interpolation without preconditioning `ch04-p-cable/seab pefp0s2,pefp0s5,pefp0s7,pefp0s9`

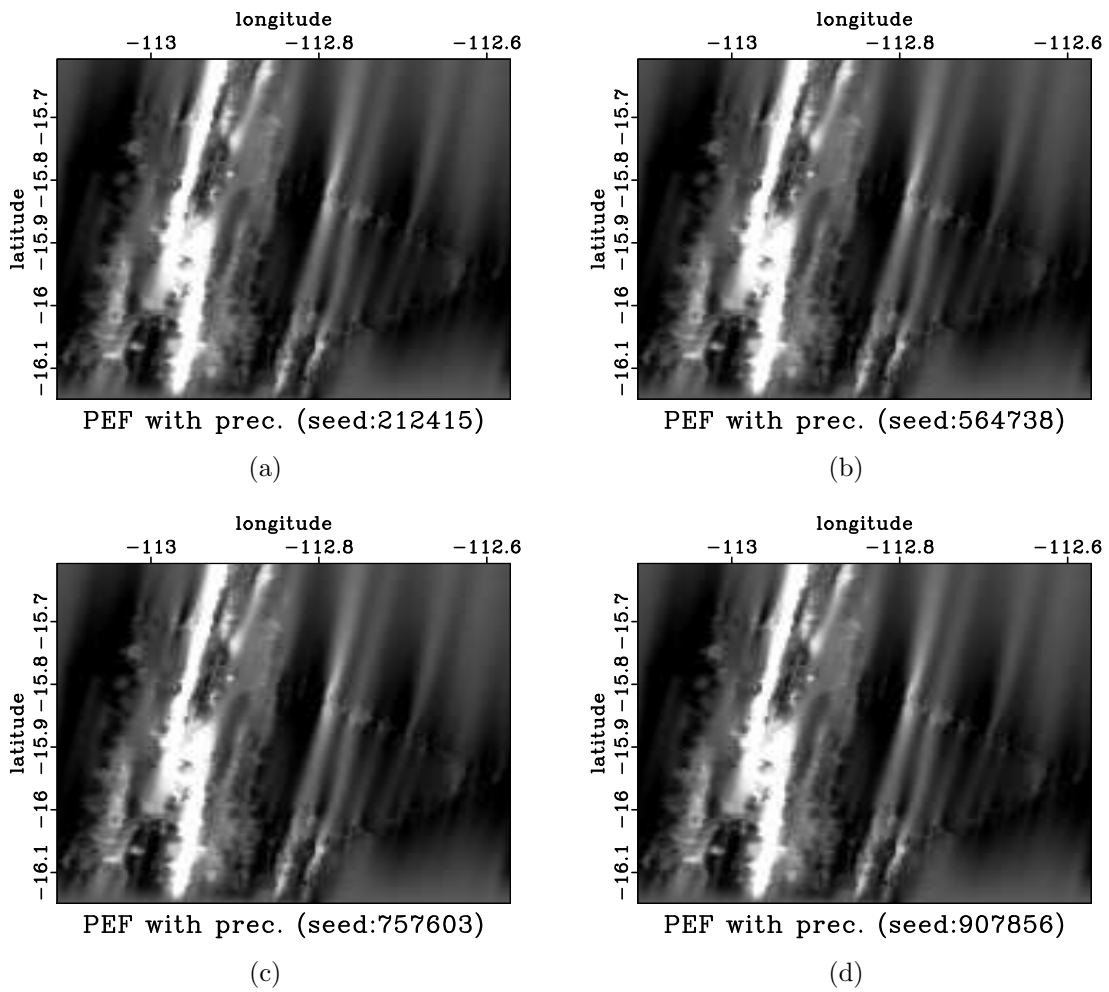


Figure 4.18: Reconstructions from the adjusted data using PEF-based interpolation with preconditioning `ch04-p-cable/seab pefp1s2,pefp1s5,pefp1s7,pefp1s9`

P-CABLE DATASET

In this section, I use seismic data from the P-cable survey — a 3-D, high-resolution, marine dataset acquired by the Gulf Coast Carbon Center at the University of Texas at Austin (Hess et al., 2014). The location is in the shallow-water transition zone off the coast of Galveston, near the San Luis Pass salt dome (Figure 4.19). The water depth is about 14 m. The survey was 26.62 km² and was acquired late in 2013. The P-cable acquisition system (Figure 4.20) uses a cable that tows 12 streamers in 12.5 m spacing each with 8 hydrophones with 3.125 m spacing sampling once every 0.5 ms. The source and receiver depths are difficult to control precisely and vary between 3 and 5 m. Noting that the common depth point bin size is 1.5625 m and the sample rate is dense, it becomes clear that the survey is high-resolution, having the ability to successfully measure frequencies up to the Nyquist at 1 kHz in this case. The expected vertical resolution is about $\lambda/4$, or 0.4 m, and horizontal resolution is approximately $\lambda/2$, or 0.8 m (calculated with an estimated water velocity of 1550 m/s).

The data have been preprocessed with noise-attenuation procedures (specifically f-k filtering and anomalous amplitude attenuation) and had the ghosts removed and designature filter applied by Hess et al. (2014). This was effective at removing most of the noise. The exception was that the acquired data suffered from semi-periodic, high-amplitude, bursts of noise. The large burst energy pollutes the original shot records nearly simultaneously (having less than 1 sample time interval separation for each trace). Armed with this information, we can conclude that the source of the noise must have been electromagnetic in nature because of the very high propagation speed needed to traverse all of the tow cables in under 500 μ s. A possible

deduced source would be that the noise was caused by electrical arcing somewhere in the ship's equipment or hardware, possibly a capacitor. This noise mostly disappears after stacking, but some remains. The burst noise becomes severely amplified when gaining the data. This is one motivation for extracting only a small shallow subset of the original data for testing with interpolation.



Figure 4.19: Map of the P-cable marine survey location `ch04-p-cable/pcableinterp` location

While collecting this survey, the air gun that was used as the source was not running at full capacity. As a result, the energy produced by the shots was less than desired. Only the first second of the data collected is usable; after that, the illumination becomes too poor to consistently distinguish real structures. For the interpolation experiments, I extracted a shallow subset of this data.

The large noticeable holes in the data have two main causes. The first is that obstacles, primarily oil rigs, were in the path of acquisition. By far, the largest source of deviation from the anticipated acquisition design was the malfunction of the global

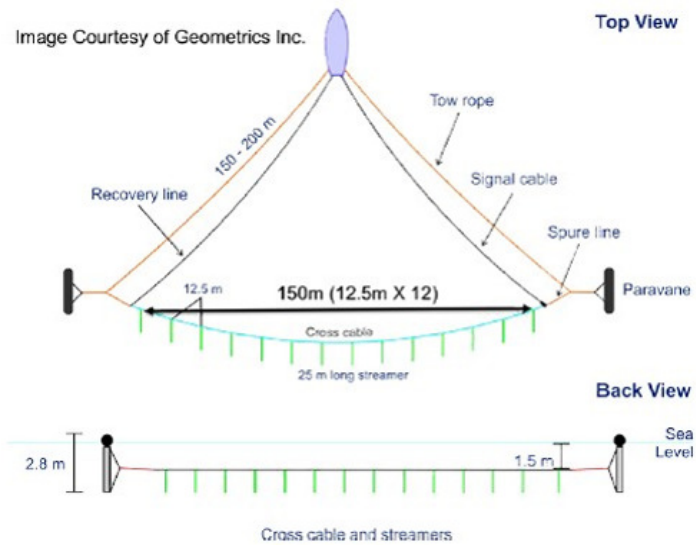


Figure 4.20: Diagram of P-cable acquisition system. Original picture by Geometrics Inc. [ch04-p-cable/pcableinterp p-acq](#)

positioning system used for marine navigation. With both of these problems working against a full fold map, massive holes litter the data.

Because of the large gaps in the fold map, interpolating across the holes in the P-cable data is necessary for some of the processing steps. The original stack data is shown in Figure 4.21. In many places, the gaps are too large for simple inline or cross-line interpolation schemes. In fact, a 2-D interpolation in any one direction would produce less-than-satisfactory results simply because of the spread of orientation of these large holes. For this reason, I use exclusively 3-D interpolation algorithms to bring in data from all sides and incorporate as much information from the data as possible. In this way, if a hole is small along any one direction the adjacent data can help fill the gap in a meaningful way.

For the P-cable data, I first make a mask, shown in Figure 4.22, with an

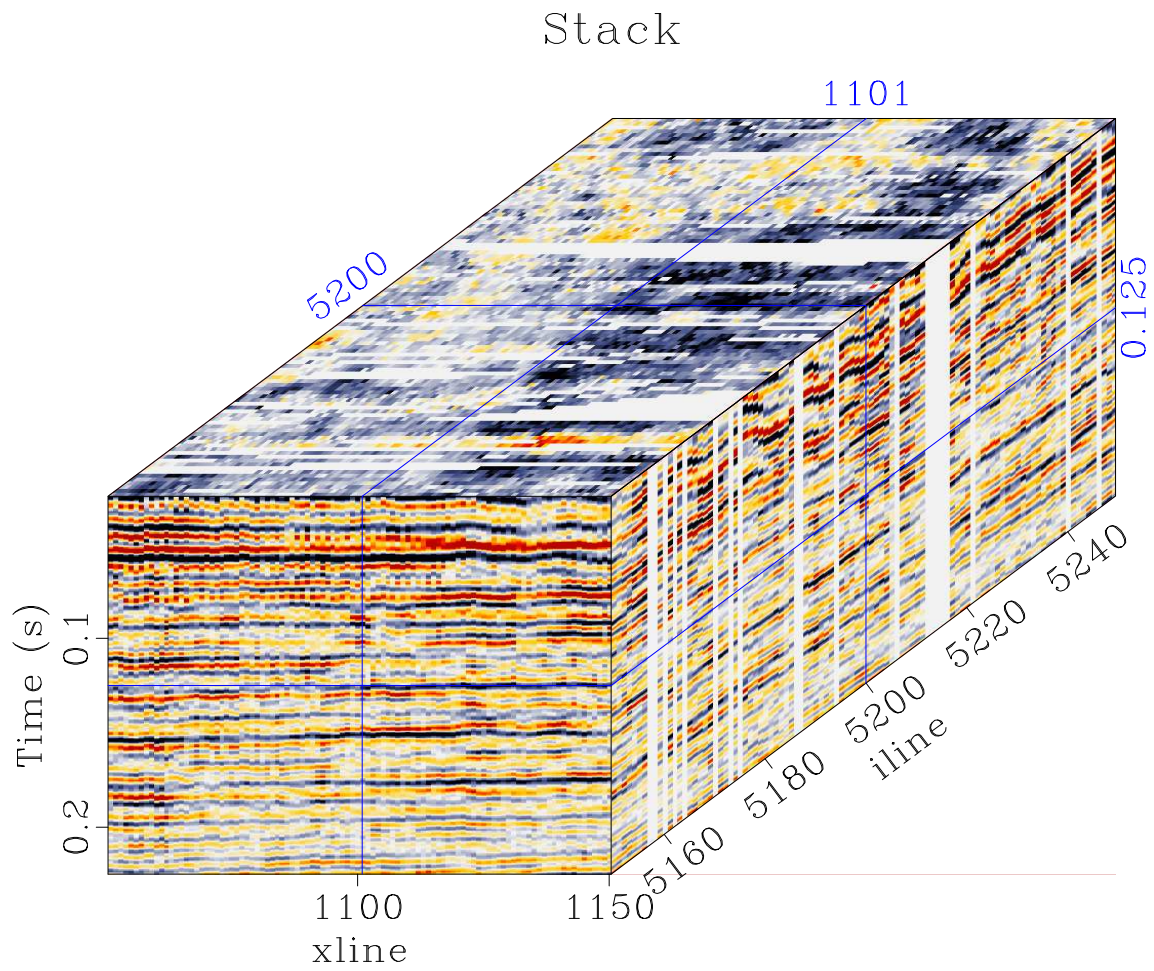


Figure 4.21: Stack of the P-cable seismic data. The large holes litter the image were created during the marine-data-acquisition phase of the project.
 ch04-p-cable/pcableinterp pc-data-3d

associated small-amplitude threshold. If the trace has amplitude values below the threshold, the mask marks it as dead (with a '0'). Inversely, live traces will have corresponding mask values of '1'. The mask makes it visually obvious to observe how much data is really missing from the original stack. Next in the interpolation process, using this mask, I estimate the dip using 3-D PWD and then use this information to predict missing values. This local slope field has two components, the inline and the cross-line (Figure 4.23). Finally, using this dip field, the original data and the mask, I can again apply plane-wave destruction or plane-wave shaping, this time to interpolate across the gaps, based on the slope, without changing the original data.

Sensitivity Analysis of Smoothing Radius

Because the true seismic response is not known everywhere, no reconstruction can be trusted with certainty. In PWS, the smoothing radius is a parameter that affects both the computational time and the relative smoothness (and thus, accuracy) of the final reconstruction. I interpolated the P-cable data with a range of smoothness values to select the most visually realistic result and depict the triangle radius's response. The findings of choosing this radius at a values of 1, 5, 10, and 20 are presented in Figures 4.24 and 4.25. Figure 4.24(a) shows that the smoothing radius of 1 is insufficient; some of the gaps in the data are too large to be accommodated by this smoothing. The smoothing radius of 20 is too large and, as a result, Figure 4.25(b) shows an artificially decreased amplitude when transitioning into the holes of missing data. A flat, side-by-side comparison of each reconstruction and the original data is presented in Figures 4.26–4.28. I conclude the smoothing radius of 5 to be the most appropriate for this data set given the need for compromise between large holes and sharp features. The radius of 10 is a bit too much because of the slight

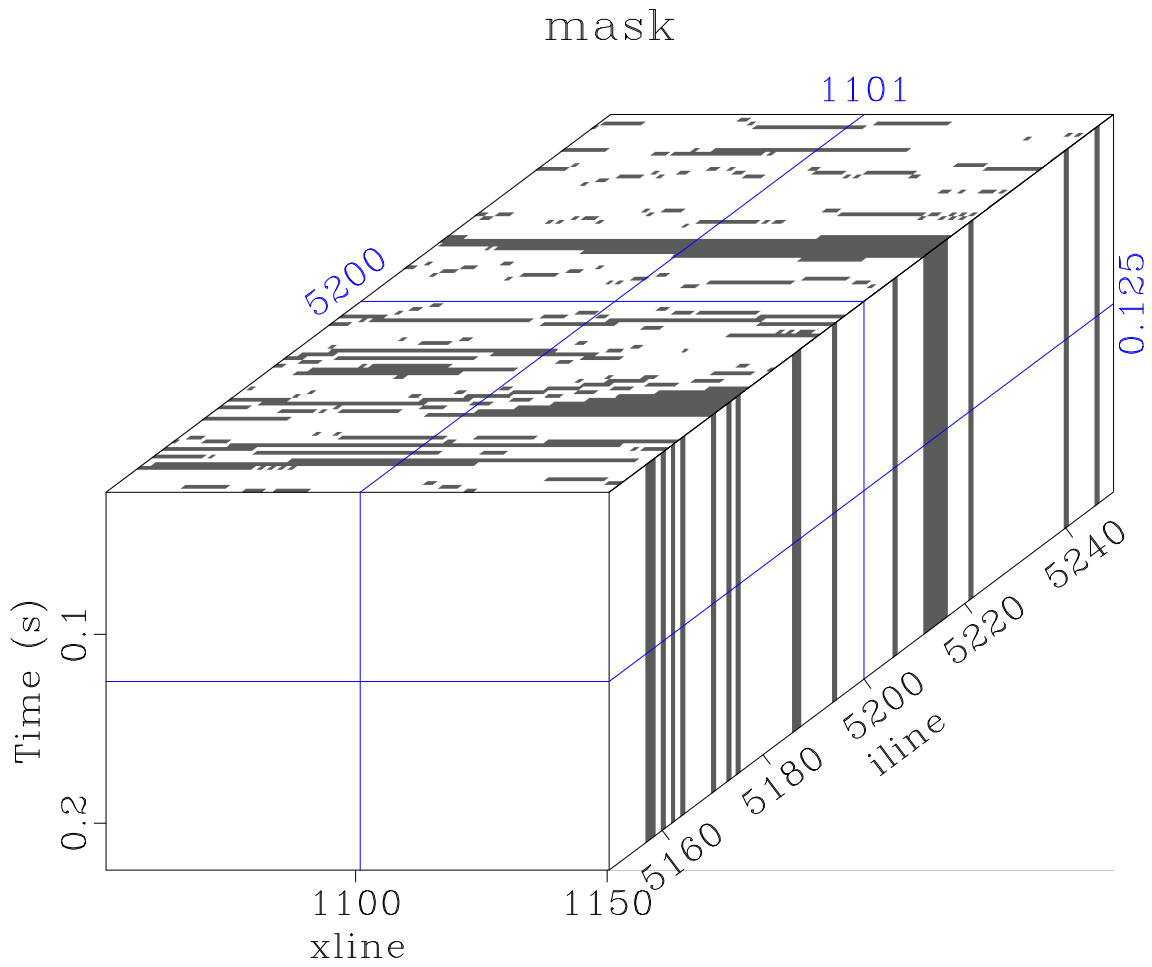


Figure 4.22: Mask of the original P-cable stack. White regions correspond to known data and have an integer value of 1. The holes in the data are black with an integer value of 0. `ch04-p-cable/pcableinterp pc-mask`

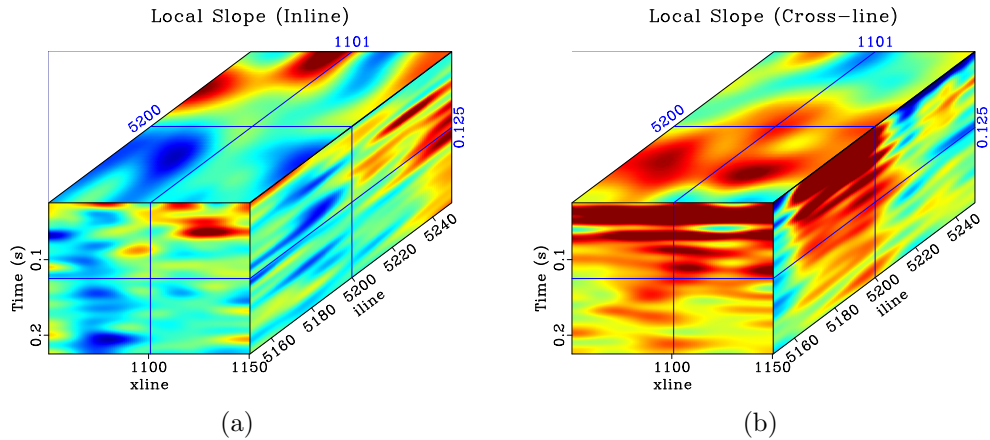
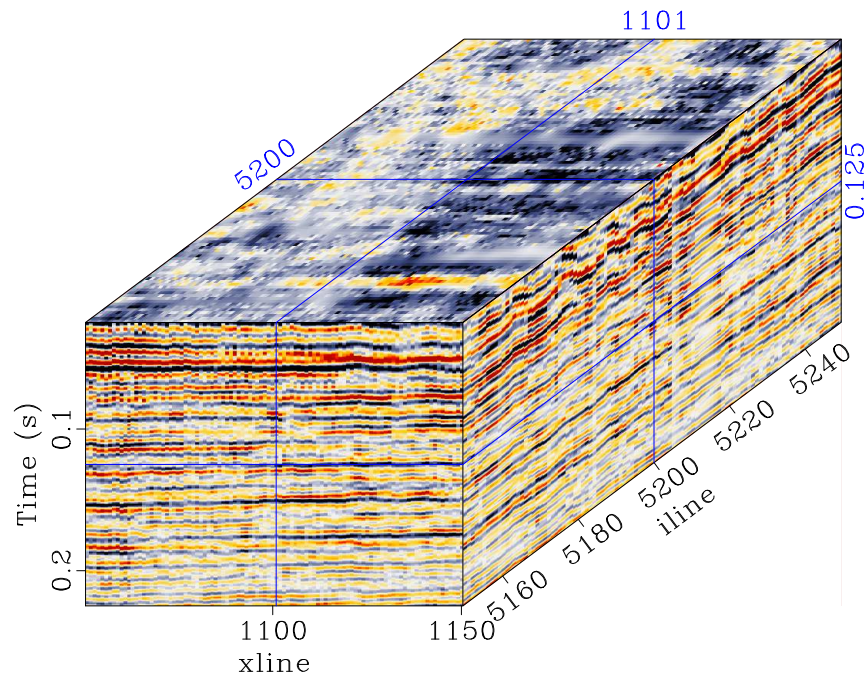


Figure 4.23: Calculated (a) inline dip and (b) cross-line dip
 ch04-p-cable/pcableinterp idip-pc,xdip-pc

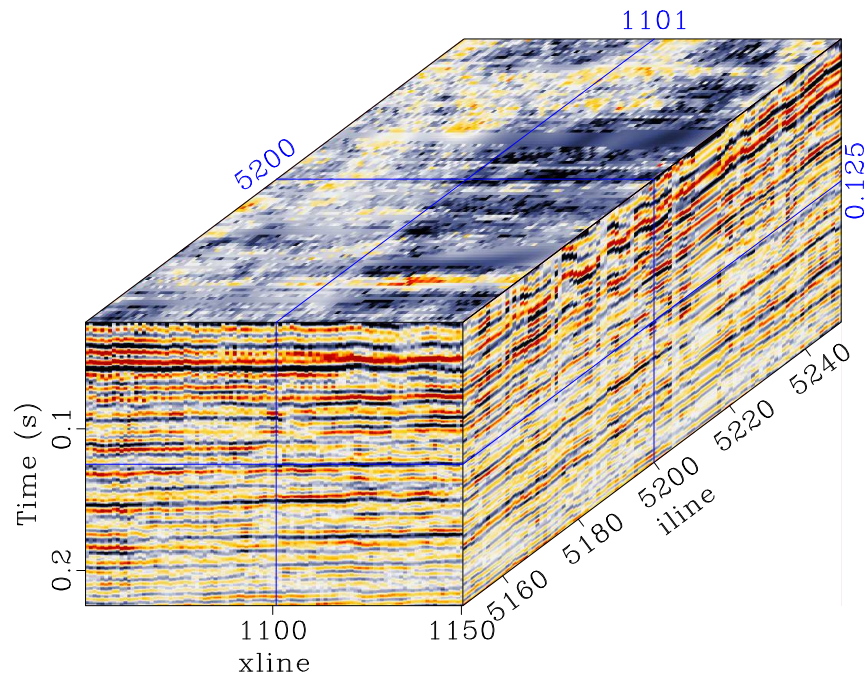
amplitude decrease and the inability to detect sharper features in the seismic data. A timeslice comparison of all of these radii with the input data and mask are given in Figure 4.29. Notice the very subtle amplitude changes in the large data gap towards the lower left. This general trend continues on: by shrinking the smoothing radius, PWS resolves sharper structures, and increasing this radius gives the ability to span larger holes such as in the SeaBeam experiment. I suggest a good rule of thumb for this process is to make the smoothing radius about the width of the data holes of the input.

Final Results and Analysis

After completing 3-D interpolation of the seismic data, I compare the results. The interpolation using the PWS-based approach is provided in Figure 4.30. Figure 4.31 shows the PWD interpolation scheme results. In some places, where the gaps are small, the PWD-based and PWS-based interpolation schemes do a decent job. I

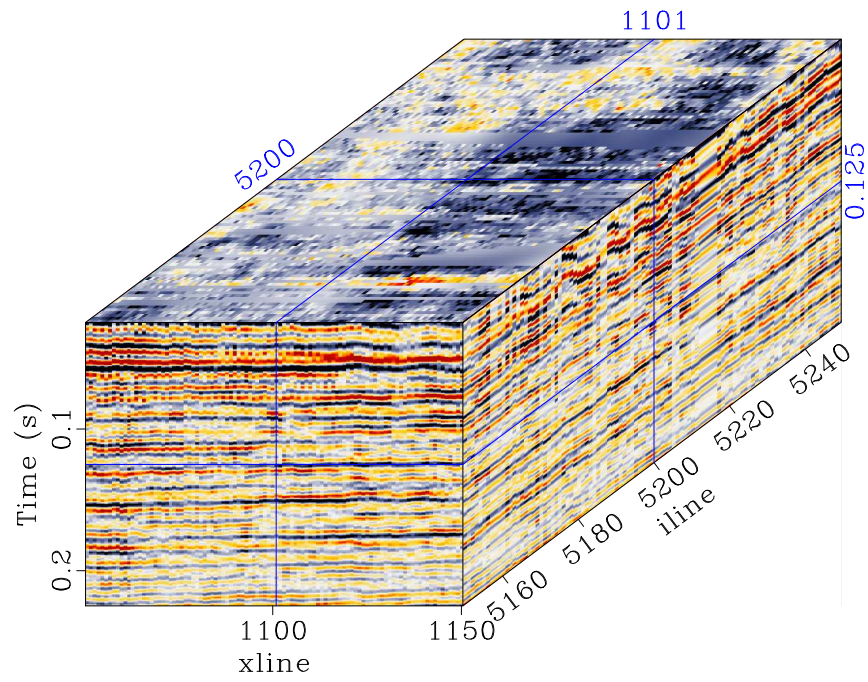


(a)

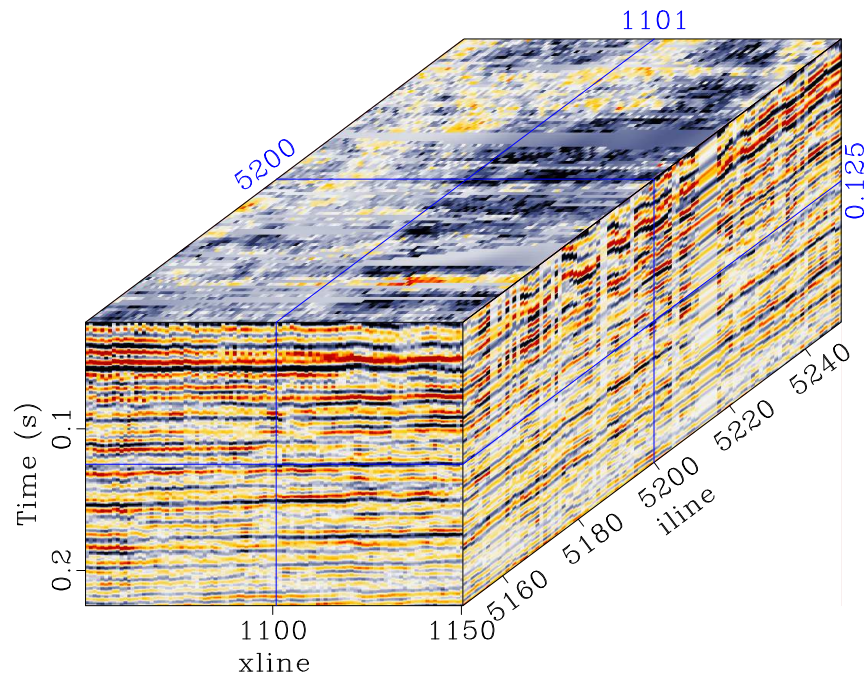


(b)

Figure 4.24: P-cable stack interpolation with smoothing radii of (a) 1 and (b) 5
 ch04-p-cable/pcableinterp pc-pws-int-o1-itr5-ns1-3d,pc-pws-int-o1-itr5-ns5-3d



(a)



(b)

Figure 4.25: P-cable stack interpolation with smoothing radii of (a) 10 and (b) 20
 ch04-p-cable/pcableinterp pc-pws-int-o1-itr5-ns10-3d,pc-pws-int-o1-itr5-ns20-3d

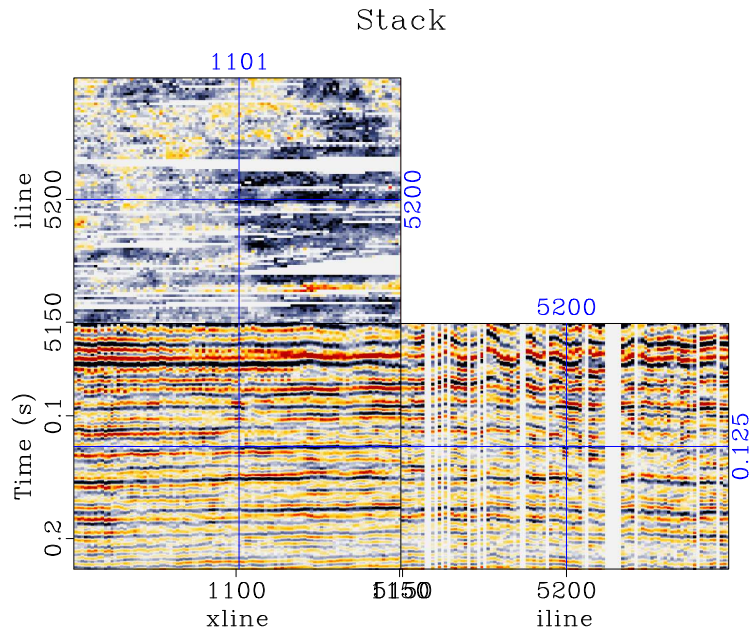


Figure 4.26: Original data flattened for display reference
 ch04-p-cable/pcableinterp pc-data-flat

can put confidence in these results by noticing that even though I used two different algorithms for deriving the interpolation, they are still consistent with each other.

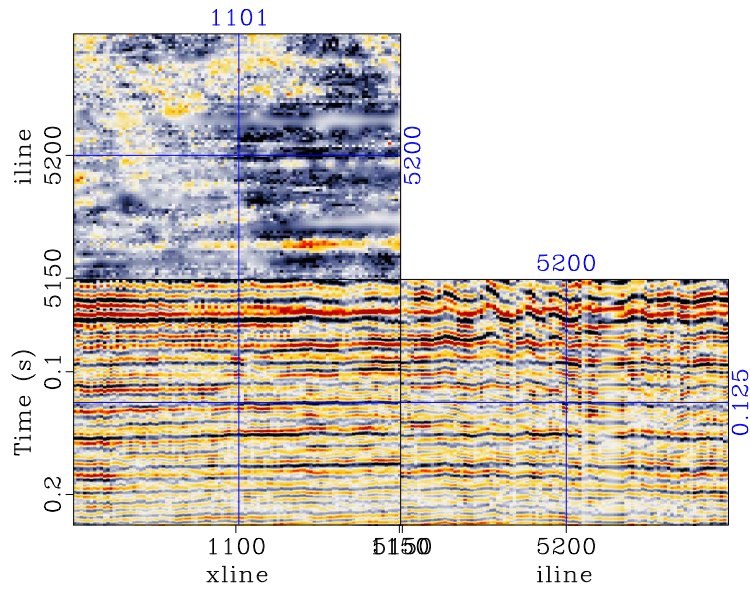
The largest holes associated with this dataset may simply be too large for a great interpolation.

Because the data started off very noisy, some additional noise attenuation flows might remove more of the electromagnetic burst energy and help give us a more accurate image.

BLAST DATASET

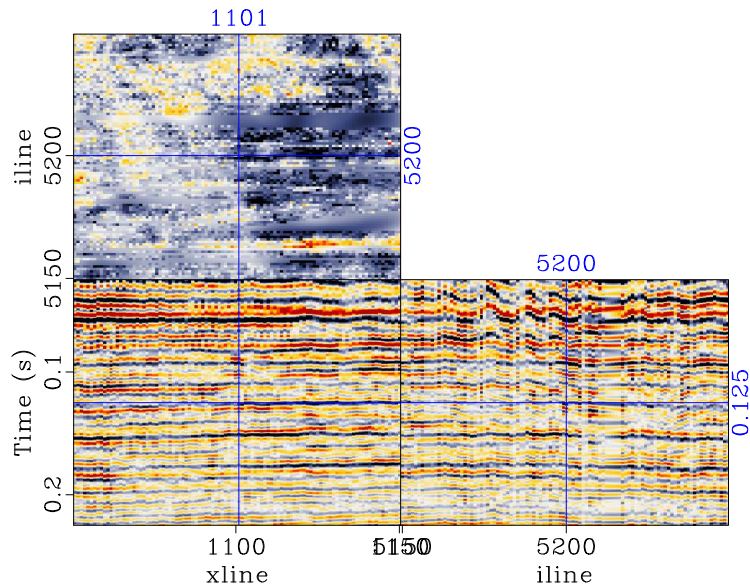
I use the Blast dataset (Figure 4.32(a)), which came from a seismic experiment with an open-pit mine-blast source, at Stanford University (Cole, 1995; Claerbout and

Missing Data Interpolation Using PWS



(a)

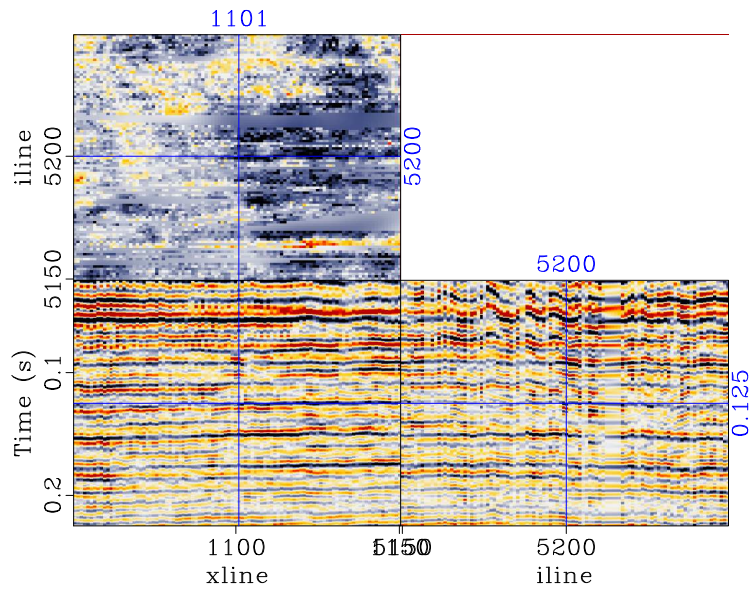
Missing Data Interpolation Using PWS



(b)

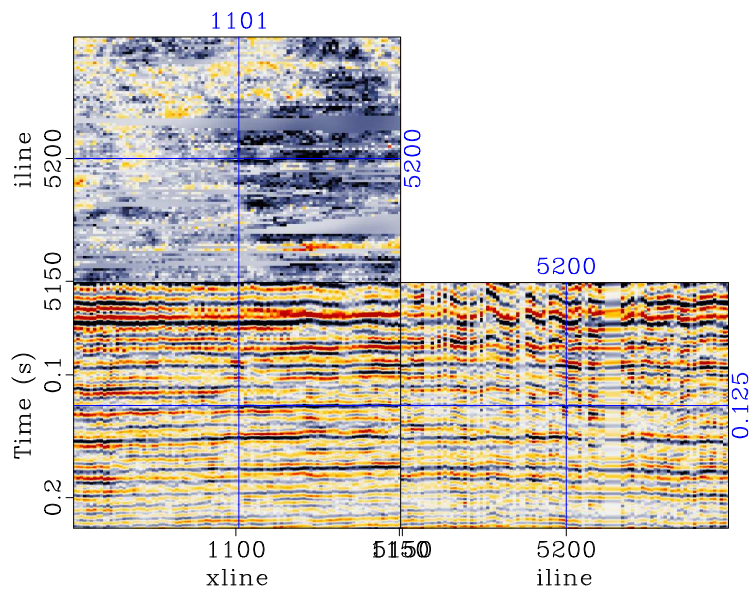
Figure 4.27: Comparison of (a) and (b) interpolation using PWS with smoothing radius of (a) 1 and (b) 5
ch04-p-cable/pcableinterp flatpc-pws-int-o1-itr5-ns1-3d,flatpc-pws-int-o1-itr5-ns5-3d

Missing Data Interpolation Using PWS



(a)

Missing Data Interpolation Using PWS



(b)

Figure 4.28: Comparison of interpolation using PWS with smoothing radius of (a) 10 and (b) 20

ch04-p-cable/pcableinterp flatpc-pws-int-o1-itr5-ns10-3d,flatpc-pws-int-o1-itr5-ns20-3d

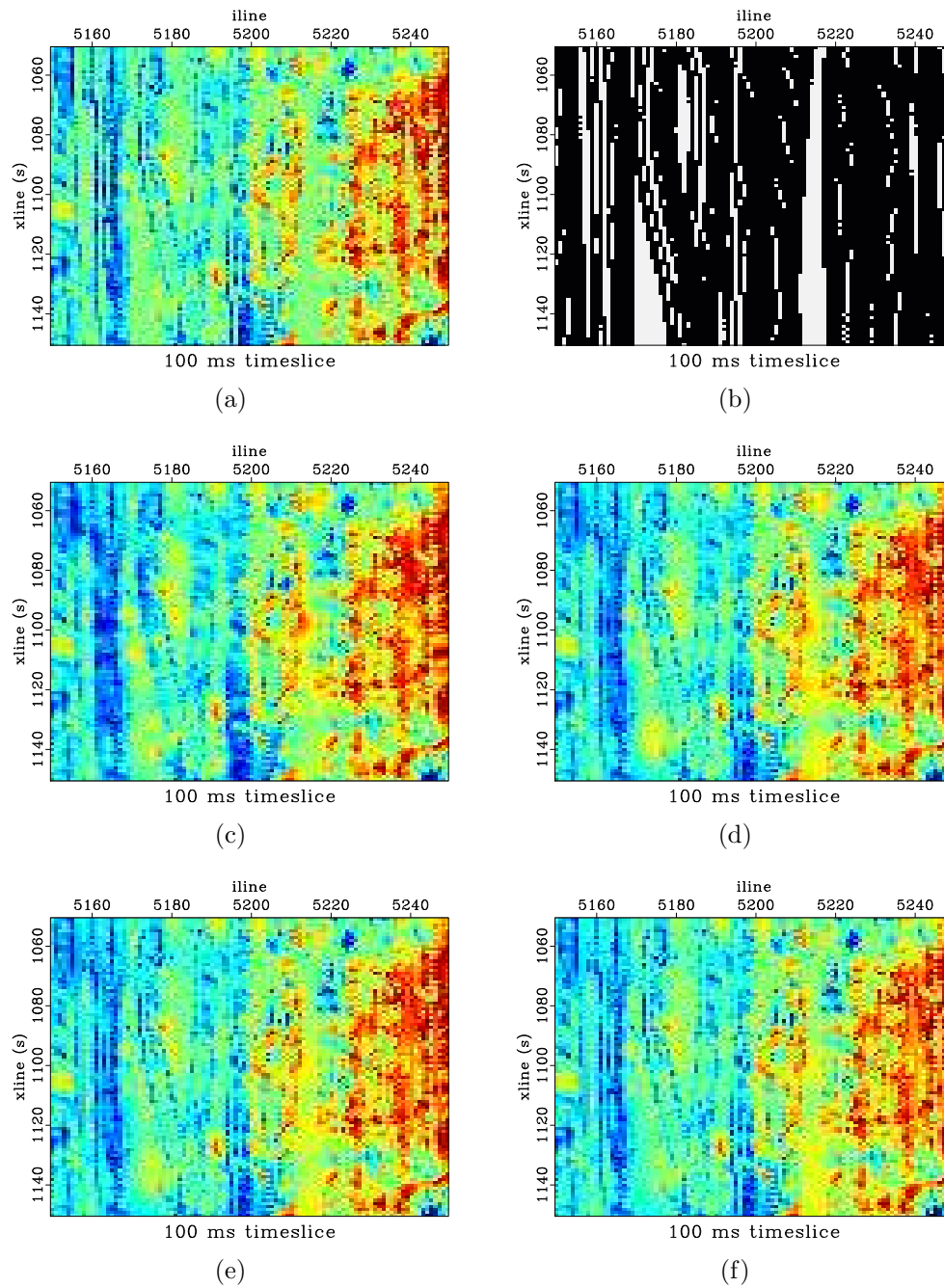


Figure 4.29: Comparison of timeslice 100 ms for (a) the original data, (b) the mask, and interpolation using PWS with a smoothing radius of (c) 1, (d) 5, (e) 10, and (f) 20.

ch04-p-cable/pcableinterp t100pcd,t100pcm,t100pcn1,t100pcn5,t100pcn10,t100pcn20

Missing Data Interpolation Using PWS

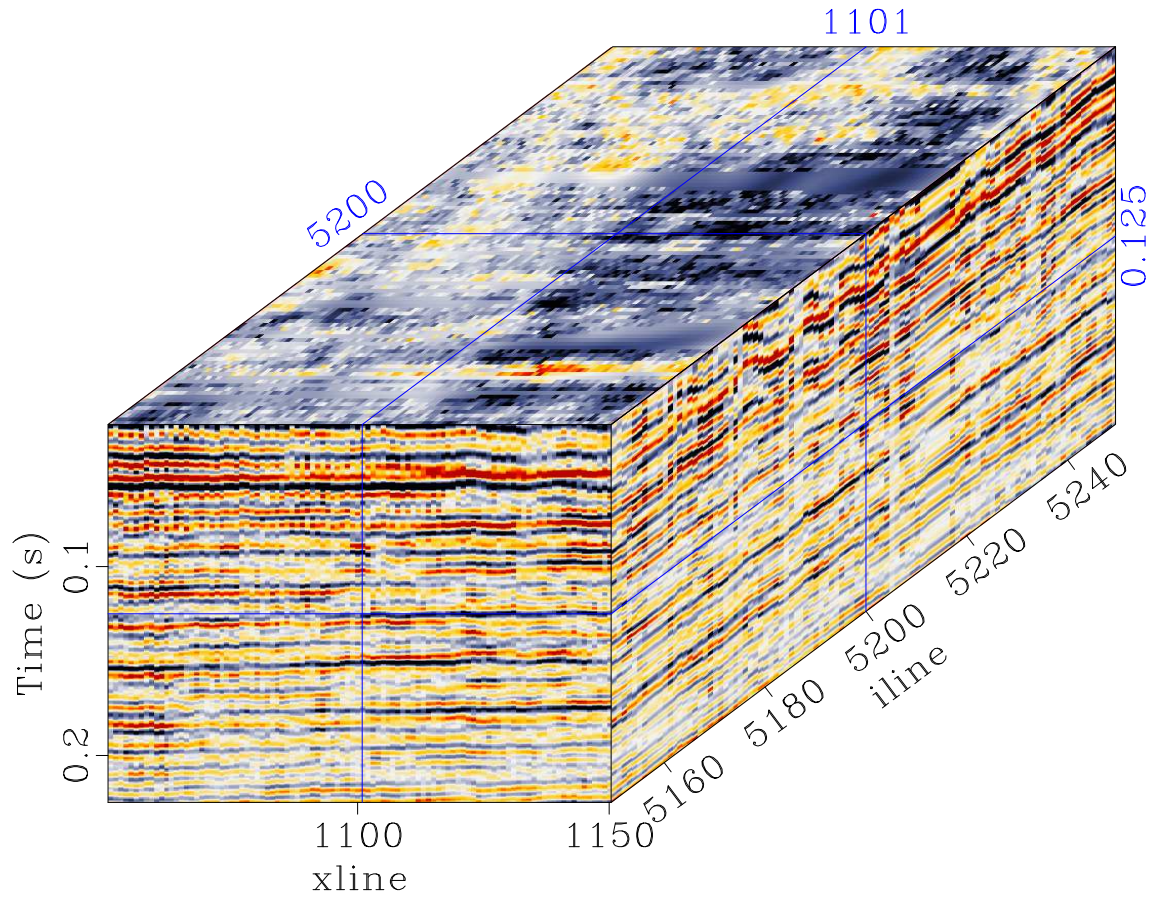


Figure 4.30: P-cable stack interpolation using 3-D PWS.
ch04-p-cable/pcableinterp pc-pws-int-01-itr5-ns5-3d-old

Missing Data Interpolation Using PWD

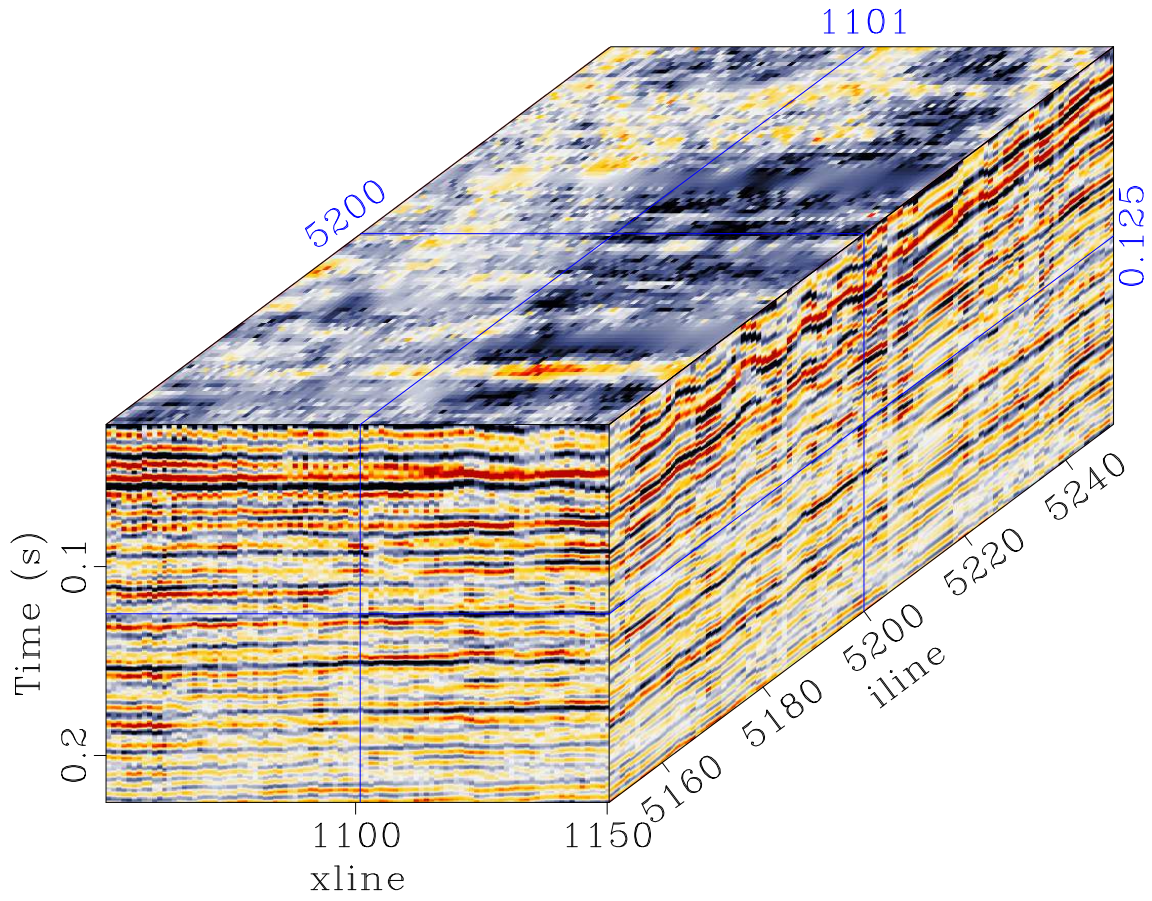


Figure 4.31: P-cable stack interpolation using 3-D PWD.
ch04-p-cable/pcableinterp pc-pwd-int-o1-3d-old

Fomel, 2014). The dataset consists of a grid of 169 receivers about half of which died during acquisition, leaving much data missing. The same 3-D interpolation schemes are used here as in the P-cable survey — PWD and PWS. The mask (Figure 4.32(b)) shows which traces are alive. From this information I calculate the dip field, in 3-D with inline dip in Figure 4.33(a) and cross-line dip shown in Figure 4.33(b).

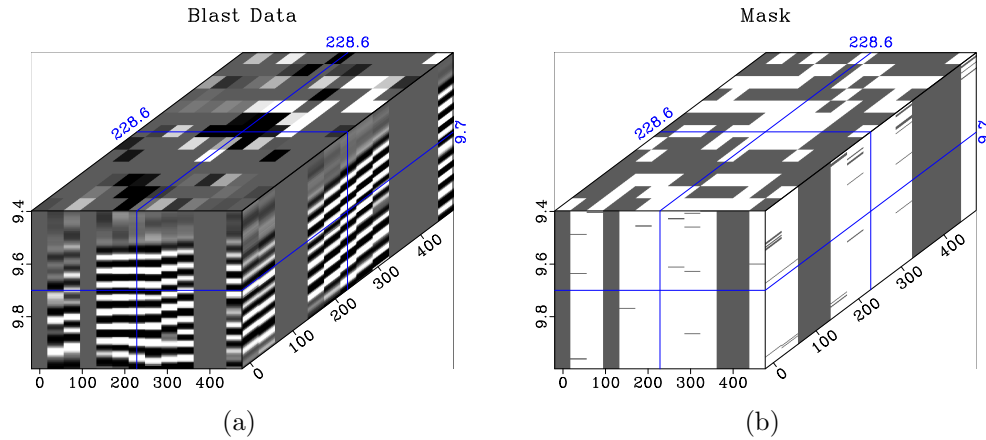


Figure 4.32: Depiction of (a) the original mine blast data and (b) its associated mask `ch04-p-cable/blast blast,blastmask`

Blast Results

After interpolation, the results between the three iterative interpolation techniques appear quite different in structure. The interpolations utilizing PWD and PWS are shown in Figure 4.34.

Because of the small size of this dataset, the panels of each can be efficiently compared with the original. This type of comparison gives a closer look at the behavior of these three algorithms. This is achieved in the panel view of Figures 4.35 and 4.36 for PWD and PWS, respectively. This style of plot reproduces the ones of Fomel (2000) and Claerbout and Fomel (2014).

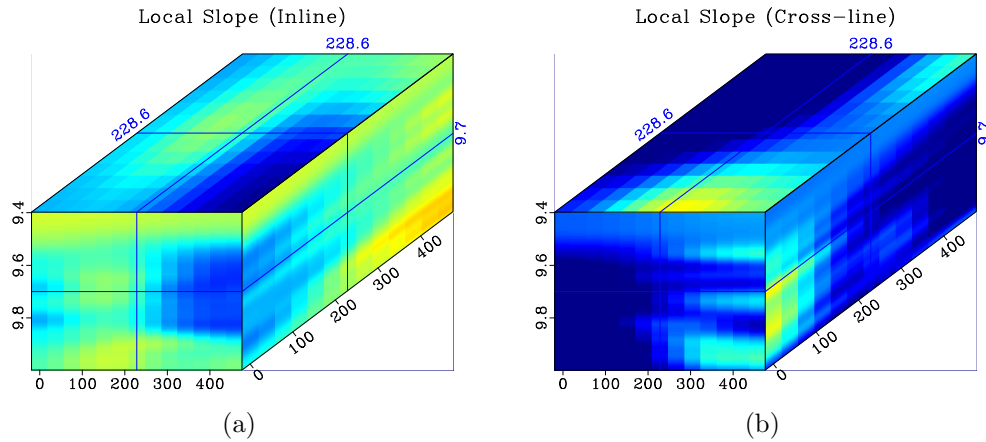


Figure 4.33: Estimated (a) inline dip and (b) cross-line dip
 ch04-p-cable/blast idip-blast,xdip-blast

Notice the sharper effect PWD appears to create in features in the data. It's impossible to know at the moment if these features are indeed geologic in nature or just artifacts of the interpolation. In the structural direction, PWS creates a slightly smoother model. The reconstruction here does not have the same ambiguities associated with PWD.

CONCLUSIONS

To summarize, I have used plane-wave shaping (PWS) in three missing-data experiments with the SeaBeam image, the P-cable marine seismic dataset, and the Blast seismic dataset. While testing the sensitivity of the reconstruction to changes in the smoothing radius of PWS, a rule-of-thumb was developed: the smoothing radius should be chosen to be about the size of the largest hole that it is tasked with filling. In a similar investigation of edge-padding, I recommend choosing a spatial padding size of half of this smoothing radius to append to both sides of the data (in

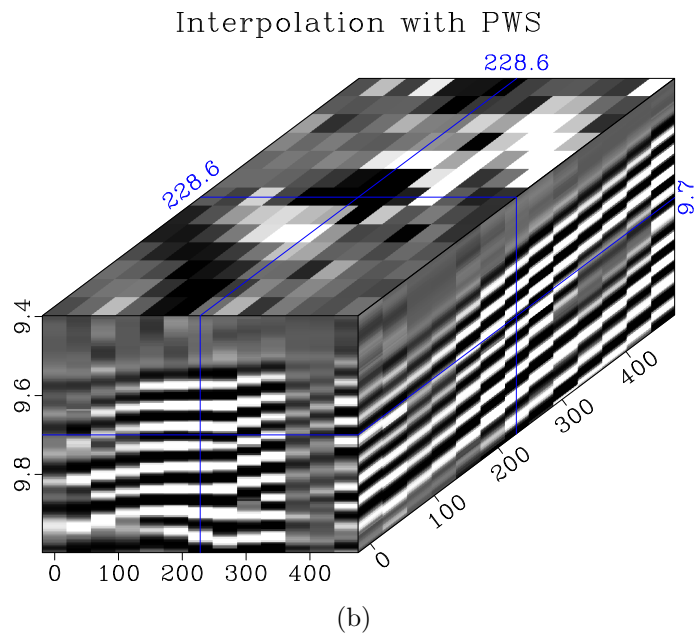
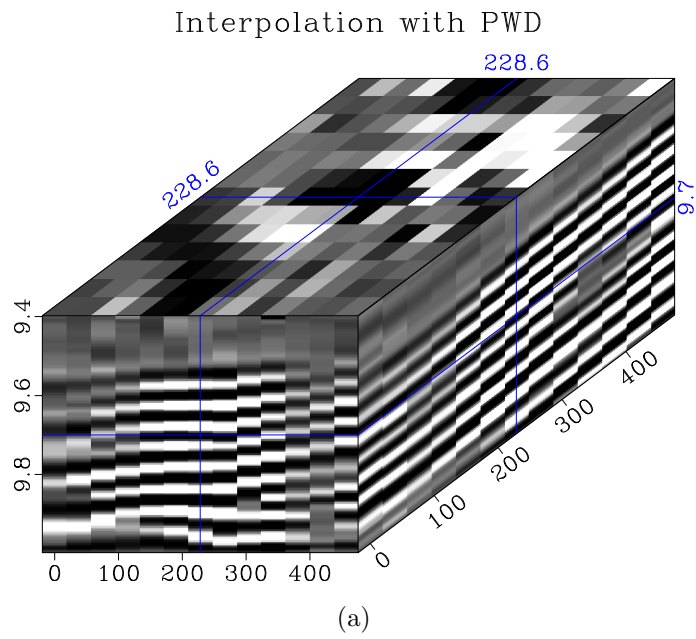


Figure 4.34: Missing-data reconstruction for the Blast dataset using (a) PWD-based and (b) PWS-based interpolation schemes
 ch04-p-cable/blast miss-pwd-blast,miss-pws-blast

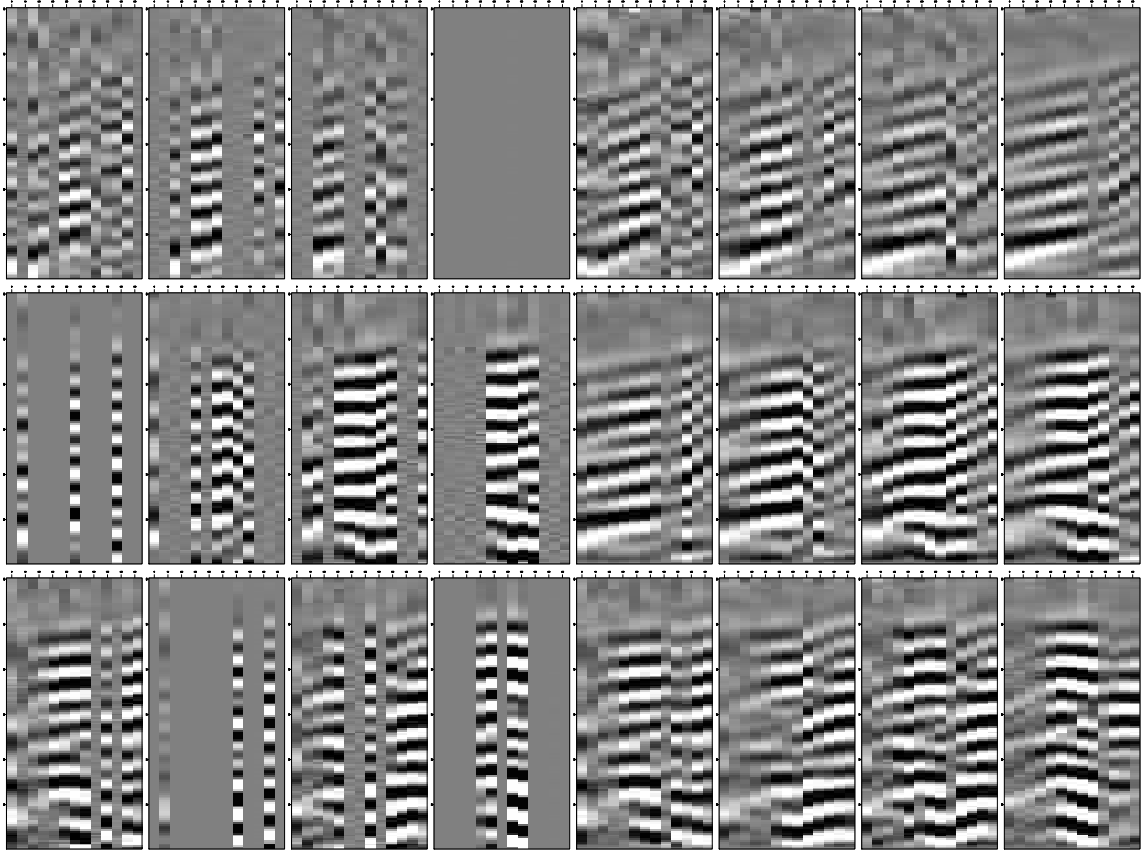


Figure 4.35: Panel view of interpolation with PWD. The left half (12 panels) of this image comes from frames of the original Blast data. The right 12 are taken after interpolating with a PWD-based approach. `ch04-p-cable/blast blast-passfill-pwd`

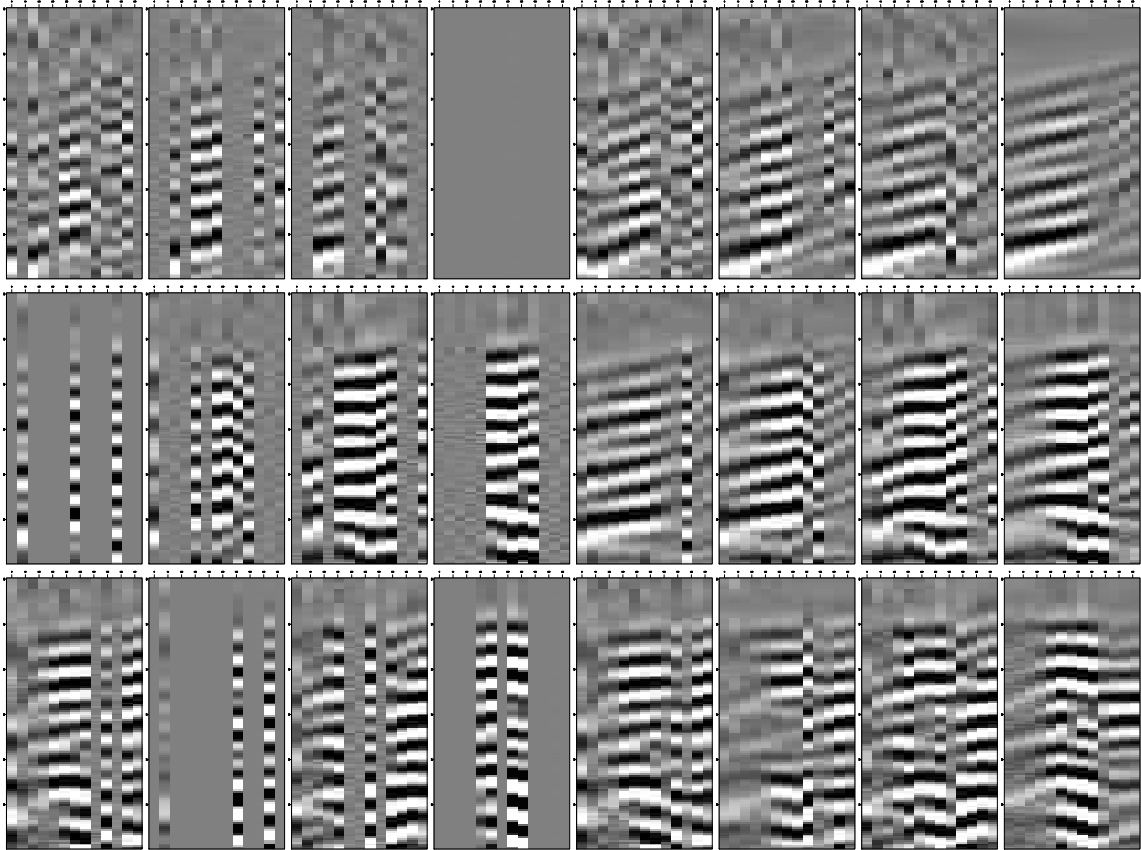


Figure 4.36: Panel view of interpolation with PWS. The left half (12 panels) of this image comes from frames of the original Blast data. The right 12 are taken after interpolating with a PWS-based approach. `ch04-p-cable/blast blast-passfill-pws`

all dimensions). The computational cost grows linearly with both of these parameters — the total data size and the smoothing radius — verifying the cost of implementation (in big O notation) as $\mathcal{O}(N_i N_r N)$.

I construct random realizations of the interpolated model that capture textural information using both PWS and PEFs. The PEF method is unable to handle the larges holes and fails at removing the acquisition footprint. The random realizations using PWS preserve pattern information and produce the most realistic results of all the methods attempted in this thesis. However, these reconstructions are highly dependent on the random noise used to generate them and might introduce artificial features in the model that can easily be unjustifiably interpreted as real geologic structures. The SeaBeam image, being 2-D, is interpolated with the 2-D versions of PWD, PWC, and PWS. The plane-wave techniques produce very similar results. The 3-D P-cable and Blast surveys were interpolated with 3-D PWD in addition to PWS. For the plane-wave methods, PWD appears to keep sharper features in the data. PWS produces a slightly smoother (in the direction of local slopes) image. The reconstruction here does not have the ambiguities associated with PWD, and the results can be more easily trusted.

Of all of the tests in this chapter, PWS converged in the fewest number of iterations compared with the alternative interpolation algorithms. PWS appears relatively stable in ability to handle a large variety of hole sizes in missing-data problems.

Chapter 5

Sobel Filter

1

Plane-wave shaping (PWS) is not limited in its use as only an interpolation scheme. It can be used to regularize a large variety of geophysical data. One additional application is incorporating PWS into an image-guided Sobel filter.

Detection, extraction, and mapping of fault planes and other discontinuities is a major challenge in the interpretation of 3-D seismic data. Visually prominent features can easily overshadow smaller features that are critical to understanding the structure and depositional environment. Seismic coherency attributes can accelerate the interpretation process by enhancing edges and providing a quantitative measure of the significance of discontinuities (Neidell and Taner, 1971; Chopra et al., 2000; Yilmaz, 2001). I propose a modification of the classic Sobel filter (Sobel and Feldman, 1968a; Kanopoulos et al., 1988) by orienting the filter along structures.

Seismic coherency attributes measure the coherence across multiple seismic traces along a horizon or time slice. Such attributes can be used to enhance previously indistinguishable faults and other geological discontinuities. These techniques provide a powerful tool for better interpretation of seismic images (Chopra and Marfurt, 2005). The first seismic coherency attribute cross-correlated each trace with its

¹Parts of this chapter appear in Phillips et al. (2015)

in-line and cross-line neighbors and combined the two results after normalizing by the energy (Bahorich and Farmer, 1995). This algorithm is very computationally efficient, but it lacks robustness. More robust coherence algorithms are more computationally expensive, as many of them require the computation of the covariance matrix (Gersztenkorn and Marfurt, 1999). The recently proposed predictive coherency attribute (Karimi and Fomel, 2013) requires multiple predictions of each trace in the seismic cube from neighboring traces.

An image that emphasizes these discontinuities can be created with the Sobel filter (Sobel and Feldman, 1968b). The Sobel filter is an edge detector that computes an approximation of the gradient at each point by convolving the data with a discrete differential operator and a triangular, moving average filter. This 2-D filter is small and integer-valued in each direction, making the Sobel filter computationally inexpensive. Different modifications of the Sobel filter have been applied previously for edge detection in seismic images (Aqrabi and Boe, 2011; Chopra et al., 2014; Luo et al., 1996) .

In this chapter, I propose to modify the Sobel filter to explicitly follow the structure of seismic horizons. This modification involves plane-wave destruction (PWD) as a differential operator (Fomel, 2002) and PWS as a smoothing filter (Fomel, 2010; Liu et al., 2010; Swindeman and Fomel, 2015). Phillips et al. (2015) tests the modification on a synthetic example and field data from the Gulf of Mexico.

Theory

The Sobel operator, \mathbf{S} , acts as a way to approximate the gradient of an image. It is defined in 2-D as the convolution of an image with two 3x3 filters. The first of

these filters amounts to triangle smoothing in the y -direction and differentiation in the x -direction,

$$\mathbf{S}_x = \begin{bmatrix} 1 & 0 & -1 \\ 2 & 0 & -2 \\ 1 & 0 & -1 \end{bmatrix} = \begin{bmatrix} 1 \\ 2 \\ 1 \end{bmatrix} [1 \ 0 \ -1] . \quad (5.1)$$

Similarly, the second filter applies the smoothing and differentiation along the opposite axes and is given by

$$\mathbf{S}_y = \begin{bmatrix} 1 & 2 & 1 \\ 0 & 0 & 0 \\ -1 & -2 & -1 \end{bmatrix} , \quad (5.2)$$

Each component of the Sobel filter is separately convolved with the data (d) to compute a low-pass isotropic approximation of the magnitude of the gradient:

$$|\nabla d| \approx \sqrt{(\mathbf{S}_x * d)^2 + (\mathbf{S}_y * d)^2}. \quad (5.3)$$

The filter behaves in a way that enhances discontinuities, acting as an edge detector (O’Gorman et al., 2008).

In the Z -transform notion, Sobel filters can be written as

$$S_x(Z_x, Z_y) = Z_x^{-1} Z_y + 2 Z_x^{-1} + Z_x^{-1} Z_y^{-1} - Z_x Z_y - 2 Z_x - Z_x Z_y^{-1} , \quad (5.4)$$

$$S_y(Z_x, Z_y) = Z_x^{-1} Z_y + 2 Z_y + Z_x Z_y , -Z_x^{-1} Z_y^{-1} - 2 Z_y^{-1} - Z_x Z_y^{-1}. \quad (5.5)$$

I propose to modify the filter for application to 3-D seismic images, where the Z_x and Z_y operators would represent not simply shifts of samples but shifts between seismic traces that follow the local plane-wave structure (Fomel, 2007, 2010). In this case, Z_x corresponds to the inline shift, and Z_y to the cross-line shift. The derivative operation is replaced with PWD (Fomel, 2002), and the triangle smoothing operation is replaced with PWS (Swindeman and Fomel, 2015). These tests are conducted by Phillips et al. (2015).

CONCLUSIONS

The Sobel filter provides a straightforward and inexpensive means for enhancing edges in seismic images and can be modified by orienting it along structure. The structure-oriented Sobel filter results in an attribute with enhanced faults. Although this attribute might not be as accurate as some of the other coherency attributes, it is much cheaper to compute. The proposed structure-oriented Sobel attribute can help improve geological interpretations of subsurface faults, channels, and other discontinuities.

Chapter 6

Conclusions

Data regularization is a useful tool for handling irregularly sampled data. Geophysics applications often require finding an appropriate solution to an ill-posed inverse problem of data regularization. This problem must be addressed appropriately before many data processing techniques can begin. I build on previous work with shaping regularization by incorporating plane-wave shaping (PWS) in two and three dimensions as a data regularization method, which can be used for the interpolation of seismic data and images.

In this thesis, I use PWS to interpolate several synthetic and field datasets and test the accuracy of image reconstruction. The image-guided interpolation scheme preserves information of geologic structures, because PWS conforms to the direction of the local slopes of an image. For comparison, I apply several alternative interpolation schemes — similarly formulated as an inverse problem with a convolutional operator to constrain the model space — namely: plane-wave destruction (PWD), plane-wave construction (PWC), and prediction-error filters (PEFs). Investigating the convergence rates, I find that PWS converges to a solution in fewer iterations than the alternative techniques. I demonstrate that the only required parameter for this method, the smoothing radius, is best selected as the same size as the largest size of the holes for missing-data problems, and the optional parameter for edge

padding should be chosen as half of the smoothing radius. Potential applications of this research include use in well-log interpolation, seismic tomography, and 5-D interpolation.

I test the effectiveness of PWS as regularization method for handling missing-data inverse problems on both real and synthetic examples. PWS is useful when constraining the estimated model parameters according to their slopes. The impulse responses of PWS filters in both 2-D and 3-D verify this image-guided nature. The quick rate of convergence of PWS is beneficial to solving large-scale, geophysical inverse problems, which might only be able to afford a small number of iterations. Of the methods tested, PWS yields the most accurate reconstruction when stopping the inversion after only a small number of iterations. Another benefit of PWS is the natural extension from 2-D to 3-D, providing high potential for practical geophysical applications beyond simple interpolation.

In Chapter 4 I task PWS with interpolating the SeaBeam image, the P-cable marine seismic dataset, and the Blast passive-seismic dataset. As the smoothing radius size and the padding size increase, the computational cost grows linearly, written as $\mathcal{O}(N_i N_r N)$ in the big-O notation, where N_i is the number of iterations, N_r is the size of the smoothing radius, and N is the size of the data. When N_i and N_r are small, the cost is linear in N .

Using both PWS and PEFs, I build noise-incorporating reconstructions that account for information that captures textural patterns. Multiple random realizations using PWS preserve structural pattern information and produce the most realistic results of all the methods attempted in this thesis. In comparison, the PEF technique was unable to handle the larger holes and failed at removing the acquisition footprint.

I used 2-D versions of PWD, PWC, and PWS to interpolate the SeaBeam image, which produced very similar reconstructions. The 3-D P-cable and Blast surveys were interpolated using both 3-D PWD and 3-D PWS. Near the edges, the reconstructions become less accurate because of the small amount of constraining information at these locations. Sharp features in the data are better preserved with PWD, while PWS produces a slightly smoother image with smoothing in the direction of local slopes. The interpolated image can be more easily trusted for PWS because it, does not have the same ambiguities as that obtained with PWD. In all of the experiments in this thesis, PWS converged in the fewest iterations of any of the alternative interpolation algorithms. PWS also appeared relatively stable in its ability to handle a large variety of hole sizes in missing data problems. PWS regularization is that it is not limited to interpolation. Some of the potential applications of this research include use in well-log interpolation, seismic tomography, 5-D seismic data interpolation, feathering correction, and seismic-discontinuity (e.g., faults and channels) detection with a structure-oriented Sobel filter.

Bibliography

- Aqrawi, A. A., and T. H. Boe, 2011, Improved fault segmentation using a dip guided and modified 3D Sobel filter: SEG Annual Meeting.
- Bahorich, M., and S. Farmer, 1995, 3-D seismic discontinuity for faults and stratigraphic features: The coherence cube: *The Leading Edge*, **14**, 1053–1058.
- Bhandari, A., A. Kadambi, R. Whyte, C. Barsi, M. Feigin, A. Dorrington, and R. Raskar, 2014, Resolving multipath interference in time-of-flight imaging via modulation frequency diversity and sparse regularization: *Optics letters*, **39**, 1705–1708.
- Boreham, D., J. Kingston, P. Shaw, and J. van Zeelsi, 1991, 3-D Marine Seismic Data Processing: *Oilfield Review*, 41–55.
- Chen, Z., S. Fomel, and W. Lu, 2013a, Accelerated plane-wave destruction: *Geophysics*, **78**, no. 1.
- , 2013b, Omnidirectional plane-wave destruction: *Geophysics*, **78**, no. 5.
- Chopra, S., R. Kumar, and K. J. Marfurt, 2014, Seismic discontinuity attributes and Sobel filtering: SEG Annual Meeting, 1625–1628.
- Chopra, S., and K. J. Marfurt, 2005, Seismic attributes – A historical perspective: *Geophysics*, **70**, 3SO–28SO.
- Chopra, S., V. Sudhakar, G. Larsen, and H. Leong, 2000, Azimuth-based coherence for detecting faults and fractures: *World Oil*, **221**, 57–64.
- Claerbout, J., 1992, *Earth Soundings Analysis: Processing Versus Inversion*: Blackwell Scientific Publications.
- , 1993, 3-D local monoplane annihilator: Stanford Exploration Project, **SEP-77**, 19–20.

- , 1999, Geophysical estimation by example: Environmental soundings image enhancement: Stanford Exploration Project.
- , 2014, Geophysical estimation by example: Environmental soundings image enhancement: Stanford Exploration Project.
- Claerbout, J., and S. Fomel, 2014, Geophysical Image Estimation by Example: Stanford Exploration Project.
- Clapp, R., 2000, 3-D steering filters: Stanford Exploration Project, **105**, 109–117.
- Clapp, R., B. Biondi, and J. Claerbout, 2004, Incorporating geologic information into reflection tomography: Geophysics, **69**, 533–546.
- Clapp, R., B. L. Biondi, S. Fomel, and J. F. Claerbout, 1998, Regularizing velocity estimation using geologic dip information: SEG Technical Program Expanded Abstracts, 1851–1854.
- Cole, S. P., 1995, Passive seismic and drill-bit experiments using 2-D arrays: PhD thesis, Stanford University.
- Daley, R., 1993, Atmospheric Data Analysis: Cambridge University Press.
- Ding, Y., and I. W. Selesnick, 2015, Artifact-free wavelet denoising: Non-convex sparse regularization, convex optimization: Signal Processing Letters, IEEE, **22**, 1364–1368.
- Engl, H., M. Hanke, and A. Neubauer, 1996, Regularization of inverse problems: Kluwer Academic Publishers.
- Fehmers, G. C., and C. F. W. Höcker, 2003, Fast structural interpretation with structure-oriented filtering: Geophysics, **68**, 1283–1293.
- Fomel, S., 1999, Plane wave prediction in 3-D: Stanford Exploration Project, **102**, 101–110.

- , 2000, Three-dimensional seismic data regularization: Stanford Exploration Project, **107**.
- , 2002, Applications of plane-wave destruction filters: *Geophysics*, **67**, 1946–1960.
- , 2007, Shaping regularization in geophysical-estimation inverse problems: *Geophysics*, **72**, R29–R36.
- , 2010, Predictive painting of 3D seismic volumes: **75**.
- Fomel, S., and J. Claerbout, 2003, Multidimensional recursive filter preconditioning in geophysical estimation problems: *Geophysics*, **68**, 577–588.
- Fomel, S., and A. Guitton, 2006, Regularizing seismic inverse problems by model reparameterization using plane-wave construction: *Geophysics*, **71**, A43–A47.
- Gao, J., A. Stanton, and M. D. Sacchi, 2015, 5D tensor-based seismic data completion: The parallel matrix factorization (PMF) algorithm.
- Gersztenkorn, A., and K. J. Marfurt, 1999, Eigenstructure-based coherence computations as an aid to 3-D structural and stratigraphic mapping: **64**.
- Hale, D., 2009, Image-guided blended neighbor interpolation of scattered data: SEG Technical Program Expanded Abstracts, 1127–1131.
- , 2010, Image-guided 3D interpolation of borehole data: SEG Technical Program Expanded Abstracts, 1266–1270.
- Hansen, P. C., 1992, Analysis of discrete ill-posed problems by means of the l-curve: SIAM review, **34**, 561–580.
- Harlan, W. S., 1995, Regularization by model redefinition: <http://billharlan.com/pub/papers/regularization.pdf>.
- Hess, T., T. Meckel, N. Bangs, and R. Tatham, 2014, Case history of acquisition and processing of a high resolution shallow water 3d multi-cable seismic survey in

- the gulf of mexico transition zone.: Presented at the 2014 SEG Annual Meeting, Society of Exploration Geophysicists.
- Hestenes, M. R., and E. Stiefel, 1952, Methods of conjugate gradients for solving linear systems.
- Kanopoulos, N., N. Vasanthavada, and R. L. Baker, 1988, Design of an image edge detection filter using the sobel operator: Solid-State Circuits, IEEE Journal of, **23**, 358–367.
- Karimi, P., and S. Fomel, 2013, Predictive coherency: SEG Technical Program Expanded Abstracts, 1492–1497.
- Li, X., and H. J. Gotze, 1999, Comparison of some gridding methods: The Leading Edge, **18**, no. 8, 898–900.
- Liu, Y., S. Fomel, and G. Liu, 2010, Nonlinear structure-enhancing filtering using plane-wave prediction: Geophysical Prospecting, **58**, no. 3, 415–427.
- Luo, X., F. Liu, S. Yang, X. Wang, and Z. Zhou, 2015, Joint sparse regularization based sparse semi-supervised extreme learning machine (S3ELM) for classification: Knowledge-Based Systems, **73**, 149–160.
- Luo, Y., W. G. Higgs, and W. S. Kowalik, 1996, Edge detection and stratigraphic analysis using 3D seismic data: SEG Technical Program Expanded Abstracts, 324–327.
- Morozov, V. A., 1971, On optimality of the discrepancy criterion in the problem of computing the values of unbounded operators: USSR Computational Mathematics and Mathematical Physics, **11**, 250–257.
- Naeini, E. Z., and D. Hale, 2014, Image and horizon-guided interpolation: SEG Expanded Abstracts, 2580–2584.

- Neidell, N. S., and M. T. Taner, 1971, Semblance and other coherency measures for multichannel data: *Geophysics*, **36**, 482–497.
- O’Gorman, L., M. J. Sammon, and M. Seul, 2008, *Practical algorithms for image analysis*: Cambridge University Press.
- Phillips, M., R. Swindeman, and S. Fomel, 2015, Structure-oriented sobel filter for edge enhancement of seismic images: SEG Technical Program Expanded Abstracts, submitted.
- Sobel, I., and G. Feldman, 1968a, A 3x3 isotropic gradient operator for image processing.
- , 1968b, A 3x3 isotropic gradient operator for image processing: Presented at a talk at the Stanford Artificial Project.
- Stanton, A., and M. Sacchi, 2012, Five-dimensional vector data interpolation: Presented at the 74th EAGE Conference & Exhibition.
- Stone, D. G., 1994, *Designing seismic surveys in two and three dimensions*: Society of Exploration Geophysicists.
- Swindeman, R., and S. Fomel, 2015, Seismic data interpolation using plane-wave shaping regularization: SEG Technical Program Expanded Abstracts, submitted.
- Tibshirani, R., 1996, Regression shrinkage and selection via the lasso: *J. Royal. Statist. Soc B.*, **58**, no. 1, 267–288.
- Tikhonov, A. N., 1963, Solution of incorrectly formulated problems and the regularization method: *IEEE Transactions on Signal Processing*.
- Woodward, M. J., D. Nichols, O. Zdraveva, P. Whitfield, and T. Jones, 2008, A decade of tomography: *Geophysics*, **73**, VE5–VE11.
- Yilmaz, Ö., 2001, *Seismic data analysis*.

Zhdanov, M. S., 2002, Geophysical inverse theory and regularization problems: Elsevier Science Publishing Co., Inc.

Vita

Ryan Swindeman grew up in Beecher, Illinois. His early academic years were spent at Beecher High School before graduating. In 2009, Ryan moved to the University of Illinois at Urbana-Champaign. There, his research was of topics in complex systems and condensed matter physics. He procured a B.S. in physics with a minor in mathematics in 2013. In 2013, Ryan began his graduate studies in geophysics at the University of Texas at Austin. He started as a member of the Texas Consortium for Computational Seismology, an initiative of the Bureau of Economic Geology and the Institute for Computational Engineering and Sciences.

Permanent address: 2215 E. Offner Rd. Beecher, IL 60401

This thesis was typeset with \LaTeX^\dagger by the author.

[†] \LaTeX is a document preparation system developed by Leslie Lamport as a special version of Donald Knuth's \TeX Program.